

University of Iceland  
RH-07-2003  
Faculty of Engineering

---

# Ultra-thin conductors and insulators

## Synthesis and characterization

by

Ívar Meyvantsson



A thesis submitted in partial satisfaction of the  
requirements for the degree of  
Master of Science in Electrical Engineering at the University of Iceland

---

Committee in charge:  
Jón Tómas Guðmundsson, Chair  
Sveinn Ólafsson  
Kristinn Johnsen

Reykjavík  
June 2003

## Abstract

In this work the electronic properties of ultra-thin metals and insulators are described, and critical structural parameters for the functionality of ultra-thin metal/insulator stacks are identified. Thin film growth is discussed with an emphasis on deposition in a magnetron sputtering discharge, and ways in which critical film parameters may be optimized. A method for film-substrate lattice matching involving the use of a binary metal alloy is discussed. Finally experimental results for a Cr-Mo alloy films down to 1.8 monolayer nominal thickness are presented.

## Útdráttur

Hér er fjallað um eiginleika ofurþunnra málma og einangrara. Bent er á þær breytistærðir sem hafa afgerandi áhrif hvað varðar virkni stafla af einangrandi og leiðandi húðum. Ræktun þunnra húða eru gerð skil. Einkum og sér í lagi notkun segulspætu og aðferðir til þess að besta afgerandi breytistærðir. Leið til samhæfingar kristalgrinda húða og undirlags, sem felur í sér notkun málmblöndu, er rædd. Að lokum eru tilraunaniðurstöður fyrir slíkar húðir, allt niður í 1.8 atómlaga þykkt, kynntar.

# Contents

<b>1</b>	<b>Introduction</b>	<b>1</b>
<b>2</b>	<b>Thin film synthesis and physics</b>	<b>3</b>
2.1	Deposition in a magnetron sputtering discharge . . . . .	4
2.2	Growth kinetics . . . . .	10
2.3	Electronic properties at the ultra-thin limit . . . . .	21
<b>3</b>	<b>Materials for ultra-thin films</b>	<b>35</b>
3.1	Metals on insulating substrates . . . . .	36
3.2	Crystalline insulators on metal substrates . . . . .	37
3.3	Metal-insulator heterostructures . . . . .	42
3.4	The $\text{Cr}_x\text{Mo}_{1-x}/\text{MgO}$ system . . . . .	43
<b>4</b>	<b>Experimental apparatus and method</b>	<b>47</b>
4.1	Magnetron sputtering discharge . . . . .	47
4.2	X-Ray Diffraction . . . . .	48
4.3	X-Ray Reflectometry . . . . .	50
4.4	Electrical resistance . . . . .	51
<b>5</b>	<b>Experimental results</b>	<b>53</b>
5.1	Experimental apparatus and method . . . . .	53
5.2	Results and discussion . . . . .	56
<b>6</b>	<b>Summary</b>	<b>63</b>

# List of Figures

2.1	A cross section of a DC glow discharge. The upper electrode is the cathode, which serves as a target for ion impact sputtering. Also shown is the substrate and power supply. . . . .	5
2.2	A cross section of a DC planar magnetron sputtering discharge. A permanent magnet is placed at the back of the cathode target with opposite poles at the center and the perimeter. The substrate sits on the anode. . . . .	6
2.3	Applied voltage waveform in a asymmetric pulsed magnetron sputtering discharge. The target is sputtered at a conventional operating voltage (a few hundred volts negative) for a fixed time. The voltage is then switched to a low positive value for a short time in each cycle.	9
2.4	Growth modes. (a) The Frank-van der Merwe mode, (b) the Stranski-Krastanov mode, and (c) the Volmer-Weber mode. . . . .	12
2.5	(a) A film of material A is deposited on a substrate of material B. (b) A flowchart for the growth mode dependence on surface and strain energies. If the surface energy, $\gamma_A$ , of the film material is considerably higher than the surface energy of the substrate, $\gamma_B$ , the three-dimensional Volmer-Weber mode will result. If $\gamma_A < \gamma_B$ , it depends on the strain which of the remaining two growth modes will appear. If the strain is negligible, the perfectly two-dimensional Frank-van der Merwe mode will result, but if the strain is considerable, its contribution $\gamma_{st}$ to the interface energy will cause islands to form on top of a two-dimensional layer after a critical thickness is reached. . . . .	13

2.6	Microstructure zone diagram for metal films deposited by magnetron sputtering. The structure is illustrated as a function of pressure, $p$ , and the ratio of the substrate temperature to the melting point $T/T_m$ [Thornton, 1986]. . . . .	15
2.7	Schematic illustration showing the steps involved in the condensation of vapor during film growth. . . . .	16
2.8	The TSK model of a surface for a simple cubic substrate. Each square represents one atom. There are two layers shown. The upper layer only covers roughly half the area shown. The edge of this layer is a step. This step separates the upper and lower terraces. The step has a kink towards the left margin. On the upper terrace is an atom adsorbed on the surface. There is also a site where an atom is missing from the layer, called vacancy. On the lower terrace four adsorbed atoms have formed an island. . . . .	18
2.9	A metal film of thickness $a$ . The film surfaces are the planes $z = 0$ and $z = a$ , and the electric field, $\mathcal{E}$ is parallel to the $x$ -axis. . . . .	24
2.10	(a) The physical structure, and (b) band diagram of a metal-insulator-metal (MIM) system. . . . .	27
2.11	Typical conduction processes in a metal-insulator-metal structure: (a) Direct tunneling, (b) Fowler-Nordheim tunneling, (c) Thermionic emission, (d) Poole-Frenkel emission, and (e) ohmic hopping conduction. . . . .	28
2.12	Diagram illustrating the thickness and electric field dependence of intrinsic conduction process occurrence (adapted from [Hori, 1997, p. 45]). . . . .	30
4.1	A magnetron sputtering discharge for ultra-thin film deposition. The vacuum chamber has three sputtering targets. . . . .	48
4.2	Apparatus for Bragg-Brentano XRD. (a) X-Ray source, (b) the sample, and (c) the detector. . . . .	49
4.3	Four-point-probe resistance measurement setup. A constant current is passed between the two outer contacts, and the voltage is measured between the two inner contacts. . . . .	51
5.1	High angle X-Ray Diffraction measurement for a $\text{Cr}_x\text{Mo}_{1-x}$ grown at $200^\circ\text{C}$ , with $x \approx 0.63$ . . . . .	54

---

5.2	X-Ray Reflectometry curves for $\text{Cr}_x\text{Mo}_{1-x}$ films, with $x \approx 0.63$ , grown at different temperatures. (a) RT, (b) 200°C, (c) 500°C, and (d) 800°C. In each figure the measured data is shown as the lower curve, and a fit to the measured data is shown as the upper curve. The curves are vertically offset for clarity. . . . .	55
5.3	Film properties for a $\text{Cr}_x\text{Mo}_{1-x}$ alloy, with $x \simeq 0.63$ . (a) Film surface roughness, (b) film/substrate interface roughness, and (c) mosaic thickness in the direction perpendicular to the substrate surface, versus growth temperature. . . . .	56
5.4	Film properties for a $\text{Cr}_x\text{Mo}_{1-x}$ alloy, with $x \approx 0.63$ . (a) Out-of-plane lattice constant, i.e. in the direction perpendicular to the substrate surface, (b) film thickness, and (c) film density, versus growth temperature. . . . .	57
5.5	Electrical resistance versus thickness for $\text{Cr}_x\text{Mo}_{1-x}$ films, having $x \approx 0.63$ , deposited at 200°C growth temperature. The inset is a magnification of the behavior in the subnanometer range. The dotted vertical lines indicate the nominal thickness of subsequent monolayer. . . . .	60



# Chapter 1

## Introduction

The number of naturally occurring elements is less than one hundred. In spite of that, a vast collection of different materials are available in the form of compounds, polymers, and alloys. The atomicity of matter was suggested by Democritus in the fifth century B.C. However, the idea was not fully established until the beginning of the twentieth century. One of the reasons may be that most frequently materials are encountered in their bulk form, where individual atoms or molecules do not play a significant role. During the past decade knowledge from various different scientific disciplines has merged to form the field of nanotechnology. Within the field of nanotechnology new materials and devices are being developed by manipulating individual atoms and molecules. The understanding of molecular behavior and the capability to construct molecules with distinctive electrical properties has led to ideas such as molecular electronics, where switches, rectifiers and interconnects are formed in a chemically synthesized molecular network. Human imagination has also been fed by the magnificent variety of molecular functionality in biological systems. A range of applications have been suggested which employ the electrical, mechanical or chemical properties of biological entities. The application of molecular building

blocks requires an interface. This is usually provided with metal electrodes. To create such electrodes, nano-lithography of some kind is needed. In recent years an effort has been made to realize nanometer lithography, with some success. However, a prerequisite for such methods to be of practical value is the ability to produce electronic materials, whose performance is of sufficient quality at nanometer length scales. Although thin film deposition equipment, such as molecular beam epitaxy (MBE) and magnetron sputtering discharge can accurately deposit amounts corresponding to single monolayers, film morphology is governed by the kinetics and thermodynamics at the surface during deposition. Film properties, that are of critical importance for nano-scale systems, are influenced by the structure. Therefore, various structural imperfections need to be eliminated. This work is concerned with insulating and conductive thin film materials, their characterization, as well as preparation methods.

In the next chapter the application of a magnetron sputtering discharge for thin film deposition will be considered, along with film growth issues, and physical properties of ultra-thin films. The third chapter covers issues regarding the choice of materials for atomic scale heterostructures. The fourth chapter presents the experimental methods applied to characterize ultra-thin metal films, and the fifth chapter reports on experimental results for  $\text{Cr}_x\text{Mo}_{1-x}$  grown on MgO.

## Chapter 2

# Thin film synthesis and physics

Thin films have found numerous applications. They serve as model systems in surface science, form the basic building-blocks of laser diodes, and provide both interconnects and passivation in integrated circuits. Thin films supported by solid substrates can offer properties not available in the bulk materials. These include superconductivity, giant magnetoresistance and various optical properties. Furthermore thin films can provide corrosion resistance, low friction, or decorative finish to objects constructed from another bulk material. Various methods have been devised to deposit thin films. These include chemical vapor deposition (CVD), where the film material is formed from gaseous precursors, molecular beam epitaxy (MBE), where the film constituents are evaporated in highly controllable amounts, and magnetron sputtering, where atoms are sputtered from a target by accelerating noble gas ions towards it. The last procedure is very established for metal deposition. A variation of it called the asymmetric bipolar pulsed magnetron discharge is widely accepted as one of the best practical methods for depositing insulating films. The first section of this chapter considers the magnetron sputtering discharge, beginning with principles of plasma discharges, then DC sputtering and planar magnetron discharges are

discussed, and finally the application of pulsed power for insulator deposition. The second section considers thin film growth in the context of the thermodynamics and kinetics at solid surfaces. In the third section the physical properties of thin film conductors and insulators are discussed.

## 2.1 Deposition in a magnetron sputtering discharge

When a substance is heated it makes a phase transition from solid to liquid to vapor and eventually to plasma. A fully ionized plasma is a collection of free charged particles moving in random directions that is, on the average, electrically neutral [Lieberman and Lichtenberg, 1994, p. 6]. The plasma transition point ranges from 4000 to 20000 K, depending on how easily the substance is ionized. This is why plasma is often referred to as the fourth state of matter. Weakly ionized plasma consists of electrons, ions, and neutral particles.

Electrically driven, weakly ionized plasma discharges have found a wide range of applications in materials processing. In such systems the electrons are not in thermal equilibrium with the ions and the neutral particles. The plasma is sustained by ionizing collisions of energetic electrons with neutral gas atoms or molecules, where only a small fraction of the gas atoms or molecules becomes ionized.

One type of weakly ionized gas discharge is the DC glow discharge. A low aspect ratio DC glow discharge for sputtering of materials is shown in Fig. 2.1 [Lieberman and Lichtenberg, 1994, p. 450]. It is commonly constructed in a cylindrical geometry, with the anode at one end and the cathode at the other. The cylinder is filled with a noble gas, typically argon, under low pressure. A negative voltage is applied to the cathode. The discharge is maintained by secondary electrons originating when positive ions impinge on the cathode after being accelerated

by the electric field. A few thousand volts are required to maintain the discharge. At such voltages the energy is sufficient for the ions to sputter atoms from the surface [Lieberman and Lichtenberg, 1994, p. 288]. The bombarding ions transfer momentum to many atoms, initiating a collision cascade. Although most of the atoms are trapped in the solid target, some may escape. The sputtering yield, i.e. the number of atoms sputtered per incident ion, depends on the cathode material and the gas used in the discharge. Influencing factors include the atomic weight ratio, and the surface binding energy of the cathode material. The atoms sputtered from the cathode have velocities distributed in all directions. In a system designed for thin film deposition, the cathode is called the target, and the rate at which a film will grow on a substrate, which is placed on the anode beneath the target, is referred to as the deposition rate.

In a DC glow discharge the high voltage required to maintain the discharge causes collisions where ions backscatter from the cathode and hit the substrate with high kinetic energy, destroying the film being formed. Also, the deposition rate is not acceptable for practical applications. A variation of the DC glow dis-

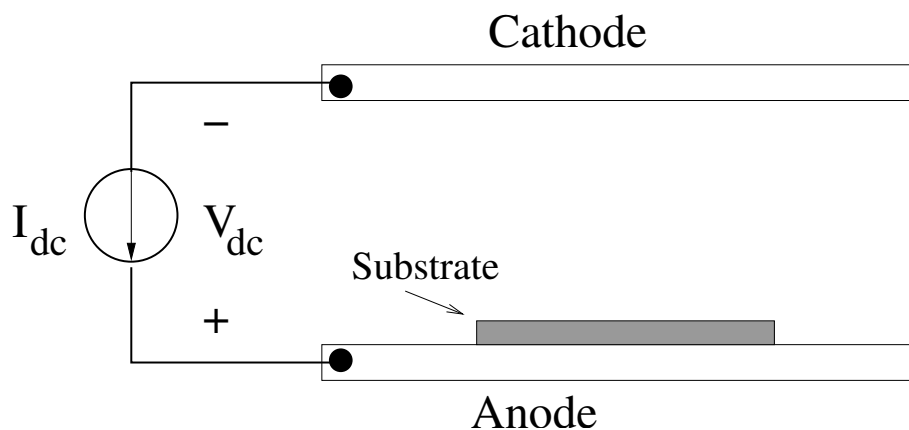


Figure 2.1: A cross section of a DC glow discharge. The upper electrode is the cathode, which serves as a target for ion impact sputtering. Also shown is the substrate and power supply.

charge, called the magnetron sputtering discharge has been developed [Waits, 1978, Lieberman and Lichtenberg, 1994, p. 465]. In the magnetron sputtering discharge, operation at a lower voltage is enabled, and at the same time, the sputtering property is enhanced in order to achieve practical deposition rates. A magnetron sputtering discharge is constructed by placing magnets behind the cathode of the DC glow discharge. Usually the magnets are arranged symmetrically behind a circular target, one at the center and the other concentrically along the perimeter. The polarity of the two magnets is such that the field lines extend from one magnet to the other, forming half a toroid. The system is illustrated in Fig. 2.2. Because of the magnetic field, the secondary electrons are trapped in a localized volume close to the target. The secondary electron trapping, in turn, increases the number of ions generated near the target, thus increasing the impingement rate of the ions on the target. This further increases the density of the secondary electrons. Consequently, the sputtering is most intensive on a circular area on the target, which has been coined racetrack [Chapin, 1974]. The result is a considerable increase in deposition rate, rendering the system practical for thin film deposition. An additional benefit of the

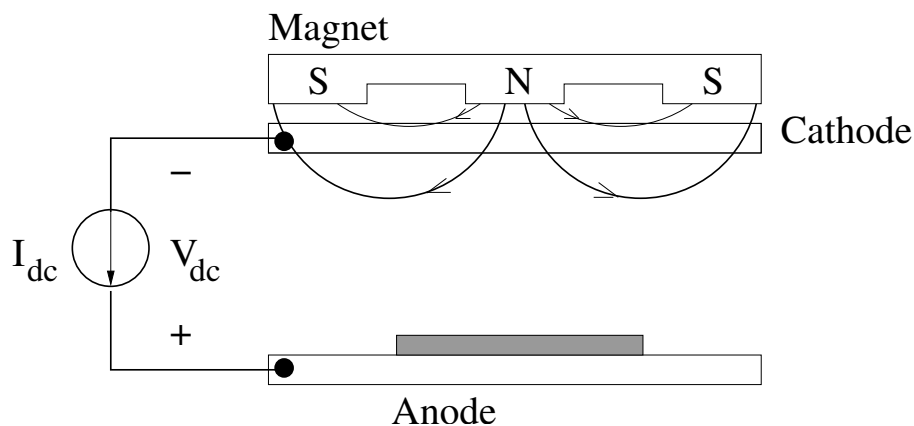


Figure 2.2: A cross section of a DC planar magnetron sputtering discharge. A permanent magnet is placed at the back of the cathode target with opposite poles at the center and the perimeter. The substrate sits on the anode.

magnetron sputtering discharge is that a lower working gas pressure can be used, thus reducing the scattering of sputtered atoms by the gas atoms. Although the sputtering primarily occurs localized on a circular area on the target, the deposited films are fairly uniform. There may be a gradient in the thickness, but that can be leveled out by rotating the substrate during growth. The thickness gradient may not pose a problem if the sample is small compared to the target.

The conventional planar DC magnetron sputtering discharge described above is widely used for the preparation of metallic films, or more generally conductive films. In order to deposit insulating films, a reactive gas may be added to the discharge, e.g. oxygen to produce oxides or nitrogen for nitride deposition. The process is referred to as reactive sputtering. For low oxygen flow rate, the gas immediately reacts with atoms sputtered from the target [Maniv and Westwood, 1980], and thus does not contribute to the pressure in the vacuum chamber. Under these circumstances oxygen doped metal films are deposited. At a critical flow rate the oxygen partial pressure sharply increases. This is when the sputtering rate of atoms from the target is no longer adequate to getter all the oxygen. Beyond this point stoichiometric oxides can be deposited. However, at this transition, oxidized regions start to appear on the target, having a marked effect on the system performance [Sellers, 1998]. For insulating oxides charge will build up on these target regions, as the impinging ions knock off secondary electrons, and some ions neutralize by removing an electron from the surface. The most intensive charge build-up occurs in regions close to the racetrack, where the density of impinging ions is relatively high, although not quite high enough to resist the formation of an oxide layer. As the surface becomes positively charged, the effective electric field is lowered. Furthermore, the sputtering yield of metal oxides is usually much lower than that of the metal due to a higher surface binding energy. For these reasons, the deposition rate is decreased.

The positive charge build-up on the target causes arcing to earthed surfaces or to other sites on the target [Kelly et al., 2000]. These two different types are called hard arcs and micro-arcs respectively. The latter can involve arcing between insulator-covered and uncovered regions or simply breakdown of the thin insulating film. Micro-arcs can usually be tolerated, whereas hard arcs are extremely detrimental to the deposition process. The conventional solution is to apply RF power to the target [Jouan and Lemperiere, 1994]. This provides process stability, but the deposition rate is extremely low. This is because sputtering will only occur while the target voltage is at a negative voltage above a certain magnitude. Thus, the duty cycle is fixed below 50% [Sellers, 1998]. Additionally, at high frequencies, less energy is transferred from the electric field to the ions. To get around this problem, asymmetric bipolar pulsing DC power supplies have been developed [Schiller et al., 1993]. In a pulsed DC magnetron discharge, the cathode is driven at a negative potential of a few hundred volts similar to its non-pulsed counterpart. However, the polarity is reversed periodically for a short time interval as illustrated in Fig. 2.3. The pulse frequency typically lies within the range 10 - 200 kHz. The time interval can be adjusted to give a duty factor from 98 down to 50 %. The amplitude of the positive pulse is usually given as a percentage of the negative operating voltage, typically 10 - 20%.

This method has several advantages. As the target turns positive, the built-up charge is dissipated through the plasma as electrons are drawn towards the target. Below a certain duty factor threshold, this eliminates arcing [Kelly et al., 2000]. The insulating layer acts as the dielectric in a capacitor, where the electrodes are formed by the target and plasma respectively [Sellers, 1998]. At the point where the target returns from the positive pulse to a negative voltage, this capacitor has been charged, and has the negative pole facing the plasma. The resulting voltage is added

to the now negative target voltage. Thus the ions in the plasma are accelerated with a higher energy towards the insulator-covered regions, than towards the uncovered target regions. This results in an increased sputtering rate of the insulating material, and is called preferential sputtering. This also helps to reduce the charge build-up. As a result of the asymmetrical waveform of the pulsed power, the average power is greatly increased compared to RF sputtering. These properties contribute to an increased deposition rate.

Thus, the magnetron sputtering discharge and its variations are powerful tools for producing both conductive and insulating films of high quality. DC magnetron sputtering allows the deposition of metal films with a precise control of deposition

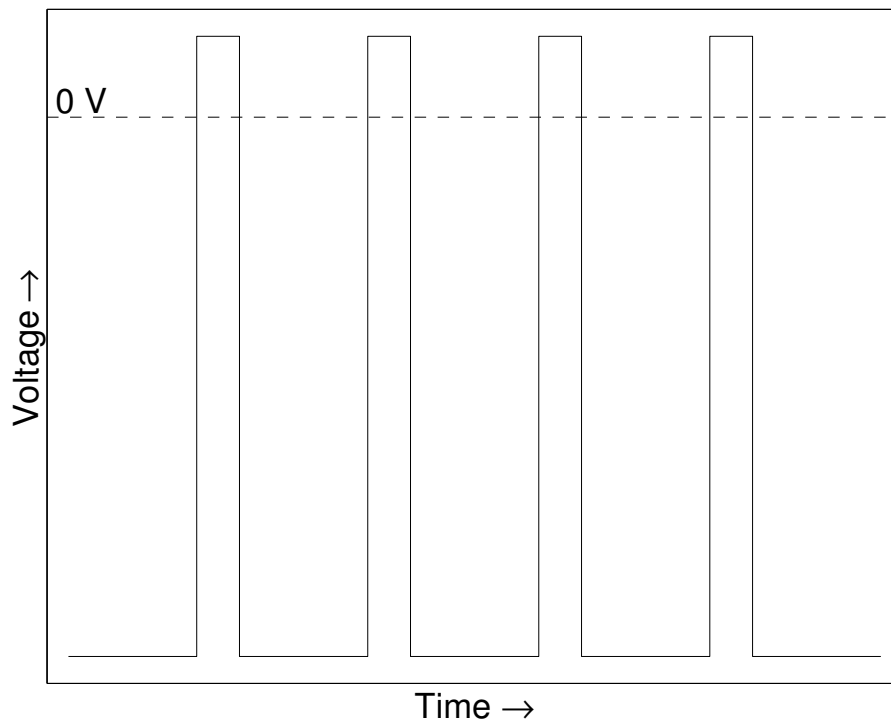


Figure 2.3: Applied voltage waveform in an asymmetric pulsed magnetron sputtering discharge. The target is sputtered at a conventional operating voltage (a few hundred volts negative) for a fixed time. The voltage is then switched to a low positive value for a short time in each cycle.

rate. The kinetic energy of sputtered atoms can have a positive influence on the film growth, as discussed below. Asymmetric pulsed power magnetron discharge offers arc free deposition of insulating films with the possibility of high deposition rates. Arc free operation reduces the film defect density by orders of magnitude [Schiller et al., 1993]. The two discharge variations can be operated together in a single vacuum chamber allowing the construction of stacked metal/insulator systems.

## 2.2 Growth kinetics

Each element and composite material possesses an equilibrium structure in its solid state. It is periodic in three dimensions and is called a crystal lattice. The crystal is bounded by surfaces, at which the periodic structure is truncated [Somorjai, 1994, p. 271 - 277]. As a result the environment of the surface atoms is quite different from that of atoms in the bulk crystal. Surface atoms have fewer nearest neighbours, and thus some bonds must be broken. Under equilibrium conditions at constant temperature and pressure the work  $\delta W$  required to increase the surface area by an amount  $\delta A$  is given by

$$\delta W = \gamma \delta A, \tag{2.1}$$

where  $\gamma$  (J/m<sup>2</sup>) is the surface tension. The surface tension is the two-dimensional analog of pressure, from a thermodynamical point of view. The surface tension is also equal to the surface free energy, and the two concepts are used interchangeably in the literature.

The heat of sublimation is closely related to the surface free energy. Sublimation involves the departure of atoms from the solid phase to the gas phase. Thus, it requires all the chemical bonds of an atom to be broken. However, the generation of a surface only requires a few bonds to be broken. Also the surface atoms form a relaxed

structure as a consequence of their less symmetric environment. In order to maximize their bonding to their remaining neighbours, they usually contract towards the bulk. Furthermore, the number of dangling bonds can be reduced by surface reconstruction, where adjacent surface atoms form additional bonds [Zandvliet et al., 2001]. Each of these effects acts to reduce the surface free energy, and therefore it is considerably less than the heat of sublimation [Somorjai, 1994, p. 271 - 277]. When a thin film of material A is deposited on a crystalline substrate of material B, different from material A, the way in which the atoms condense on the surface is influenced by the surface energies of the two materials, the accommodation of misfit strain, and the chemical interaction between A and B [Barnham and Vvedensky, 2001, p. 29]. The latter two properties are described by the interface energy,  $\gamma_{\text{in}}$ , and the surface energies of A and B are given by  $\gamma_{\text{A}}$ , and  $\gamma_{\text{B}}$ , respectively. Under certain conditions, the atom arrangement is determined by the substrate crystal surface, i.e. the crystallographic order of the film being formed is influenced by that of the substrate. This is called epitaxy, and has many advantages compared to polycrystalline films [Smith, 1995, p. 226]. Epitaxial growth eliminates grain boundaries, allows control over film crystal orientation, provides potential for atomically smooth growth, and enables atomic scale structure definition.

Atomically smooth epitaxial growth can not always be realized at the quasi-equilibrium conditions that are necessary for the film to reach good crystalline order [Bauer and van der Merwe, 1986]. Near equilibrium, thin crystalline films grow by one of three mechanisms, depending on the relative magnitudes of the surface energies,  $\gamma_{\text{A}}$  and  $\gamma_{\text{B}}$ , and of the interfacial energy  $\gamma_{\text{in}}$ . These are the Frank-van der Merwe (FM), the Stranski-Krastanov (SK), and the Volmer-Weber (VW) modes. Monolayer-by-monolayer growth occurs only in the FM mode, illustrated in Fig. 2.4

(a), which is actualized when

$$\gamma_A + \gamma_{in} \leq \gamma_B, \quad (2.2)$$

independent of film thickness. The interfacial energy includes a strain component,  $\gamma_{st}$ , which can increase with each additional monolayer, thus the condition can break at some critical thickness. That way a finite number of smooth monolayers are formed after which growth proceeds with three-dimensional island formation to accommodate lattice mismatch. This is the SK mode, illustrated in Fig. 2.4 (b). If the condition presented in equation (2.2) is unfulfilled from the very beginning, then three-dimensional crystals form immediately and the film does not become continuous until a critical thickness of several or even tens of monolayers is reached. This is the VW mode, illustrated in Fig. 2.4 (c). A flowchart describing the appearance of the different growth modes is given in Fig. 2.5

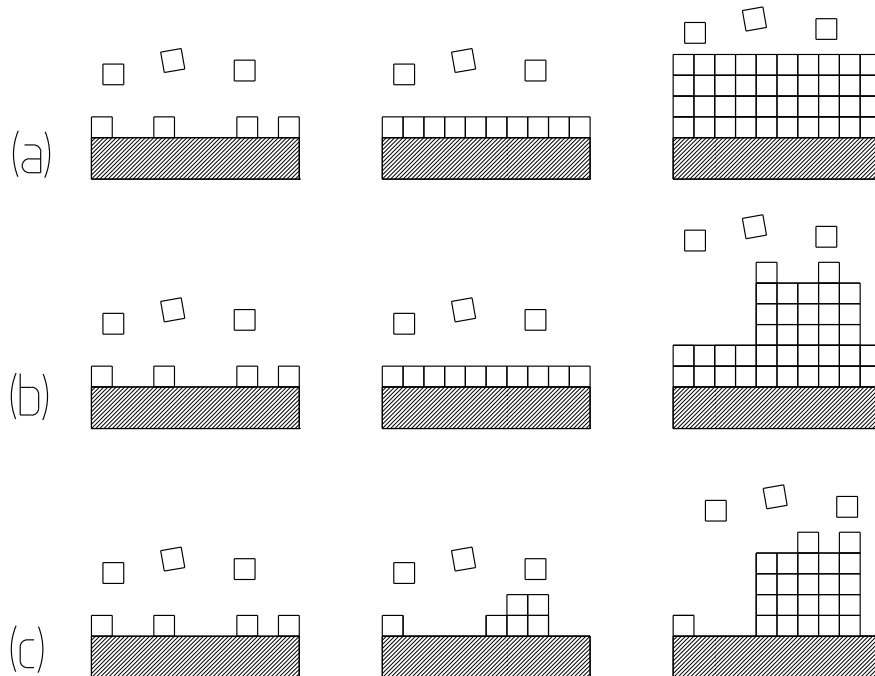


Figure 2.4: Growth modes. (a) The Frank-van der Merwe mode, (b) the Stranski-Krastanov mode, and (c) the Volmer-Weber mode.

For the purpose of nanometer and sub-nanometer interconnects, it may be required to construct a stack of alternating insulating and conductive films. As discussed above, epitaxial growth is very desirable. An epitaxial multilayer stack is referred to as a superlattice. If  $\gamma_A$  and  $\gamma_B$  differ strongly, the material with the higher surface energy will form three dimensional crystals, thus disabling the formation of a smooth superlattice [Bauer and van der Merwe, 1986].

The design of a two component stacked thin film system involves not only the choice of the two materials, but also the choice of their epitaxial relationship defined by the orientation of the substrate. Surface energies differ considerably between different crystal faces [Wang et al., 2000], which brings us to one of three ways in which a smooth superlattice can be constructed. The choice of epitaxial relationship can be used to minimize the difference in surface energy. If, additionally, the

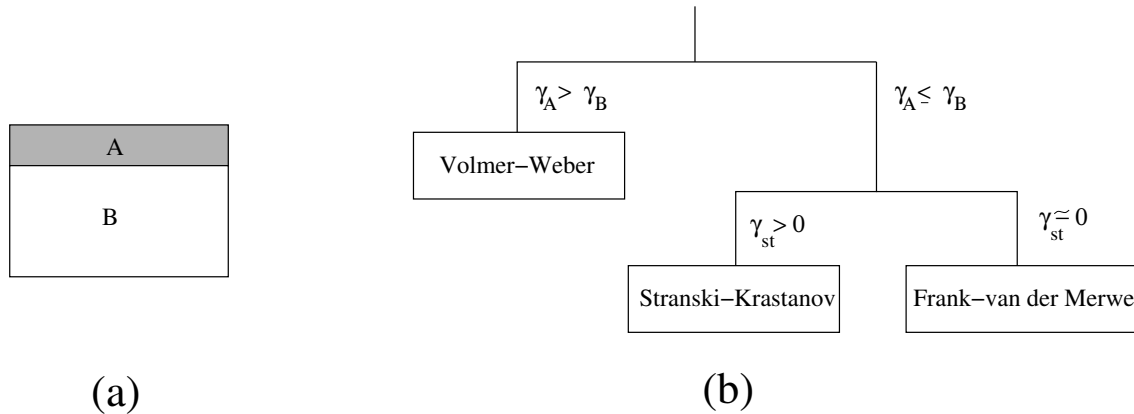


Figure 2.5: (a) A film of material A is deposited on a substrate of material B. (b) A flowchart for the growth mode dependence on surface and strain energies. If the surface energy,  $\gamma_A$ , of the film material is considerably higher than the surface energy of the substrate,  $\gamma_B$ , the three-dimensional Volmer-Weber mode will result. If  $\gamma_A < \gamma_B$ , it depends on the strain which of the remaining two growth modes will appear. If the strain is negligible, the perfectly two-dimensional Frank-van der Merwe mode will result, but if the strain is considerable, its contribution  $\gamma_{st}$  to the interface energy will cause islands to form on top of a two-dimensional layer after a critical thickness is reached.

lattice mismatch is only slight, and if the two materials exhibit a strong attractive interaction, this may result in negative interfacial energy, which may be enough to outweigh the surface energy difference and thus fulfill the condition for FM growth presented by equation (2.2) [Chambers, 2000]. If this is insufficient, and the difference is still too high, the problem may be solved with the aid of a surface active agent (surfactant). A surfactant is a medium which may be used to modify the surface energy. By exposing the surface of the high-surface-energy component to a surfactant, the surface energy may be lowered, possibly enabling growth in the FM mode. Surfactants can also modify atomistic processes in thin film growth as discussed below [Zhang and Lagally, 1997]. Surfactants are usually chosen so that they are immiscible in the film. That way a negligible amount is incorporated in the film and the surfactant is easily removable after the growth is completed. The third method for inducing superlattice formation at a finite surface energy difference is to give up quasi-equilibrium conditions [Bauer and van der Merwe, 1986]. By increasing the deposition rate or decreasing the substrate temperature, the nucleation rate in the SK and even in the VW mode can be made large enough for the three-dimensional crystals to merge into a continuous multilayer before the desired thickness is reached. Non-equilibrium films of this kind have been shown to be unstable, and exhibit aging on a timescale of minutes [Byon et al., 2003]. Nonetheless there may be a possibility that the film structure can be "frozen in" by the next multilayer in the stack [Ostadal and Hill, 2001], thus enabling the growth of smooth superlattices. When the film has been covered by a new layer in the stack, it is no longer on the surface, and thus the thermodynamic driving force for three-dimensional island formation is no longer present. As a general rule, metals grow in the VW mode on insulating substrates [Jalochowski and Bauer, 1988]. Thus, methods to induce smooth film growth under these circumstances are extremely important for the current objective

to obtain ultra-thin metal/insulator stacks.

The influence of deposition rate and substrate temperature discussed above emphasize the fact that film growth is not entirely determined by the thermodynamics. Rather, it is a non-equilibrium phenomenon governed by competition between thermodynamics and kinetics [Zhang and Lagally, 1997]. These parameters can modulate the film structure in either a positive or a negative manner relative to that dictated by thermodynamics. Thus it is critical for film quality that these parameters be adjusted to sensible values. The dependence of the microscale structure and topography on the substrate temperature and gas pressure for metal films deposited by magnetron sputtering was mapped by Thornton [Thornton, 1974, Thornton, 1986]. There are several factors that distinguish sputtering from evaporation-based deposition techniques. The most important differences lie in the high kinetic energy of

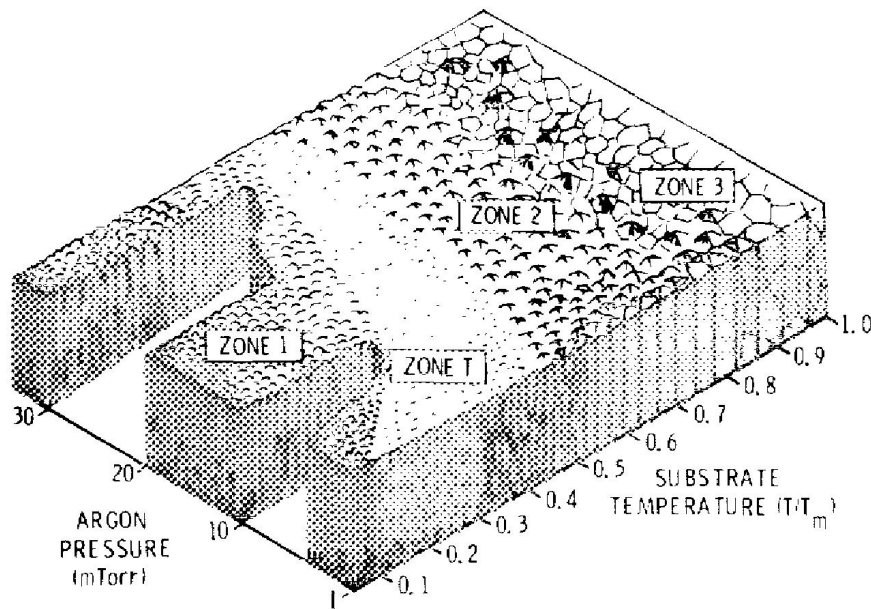


Figure 2.6: Microstructure zone diagram for metal films deposited by magnetron sputtering. The structure is illustrated as a function of pressure,  $p$ , and the ratio of the substrate temperature to the melting point  $T/T_m$  [Thornton, 1986].

the sputtered atoms, and the continuous presence of ambient gas. In a magnetron sputtering discharge, the gas pressure influences the energy of the deposited atoms, and can thus have a marked effect on the film properties as discussed below. Thornton presented his observations in terms of the temperature ratio  $T/T_m$ , where  $T$  is the substrate temperature during deposition and  $T_m$  is the film material melting point. His findings are summarized in Fig. 2.6. At very low  $T/T_m$ , where surface mobility is negligible, the films were found to consist of tapered crystallites separated by voids (zone 1). This structure tends to persist to higher  $T/T_m$  values as the sputtering gas pressure is increased. At higher  $T/T_m$  values, the structure passes into a transition zone characterized by tightly packed, short fibrous grains (zone T) which increase in both width and length with increased  $T/T_m$  and exhibit a relatively smooth surface. This zone covers a relatively large range of  $T/T_m$  values and is the prevailing low-temperature structure for low pressure operation. Beyond this region, at temperatures high enough for surface mobility to become significant, i.e.  $T/T_m > 0.3 - 0.5$ , columnar grains appear (zone 2). They initially have faceted surfaces, but at even higher  $T/T_m$  they develop into smooth flat grains with grooved boundaries (zone 3). Here the temperature is high enough for considerable bulk annealing to take place. In the high  $T/T_m$  range the structure is independent of gas pressure.

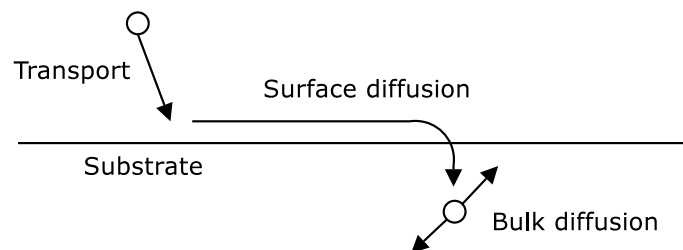


Figure 2.7: Schematic illustration showing the steps involved in the condensation of vapor during film growth.

Film growth can be envisioned as proceeding in three steps as illustrated in Fig. 2.7. The first step involves the transport of sputtered atoms to the substrate. The second step involves the adsorption of the atoms onto the surface, their diffusion along this surface and finally incorporation into the growing film, or possibly their removal by evaporation or sputtering. The third step involves bulk diffusion and other processes by which the atoms assume their final position within the film.

The appearance of tapered crystallites and voids at low substrate temperature ( $T/T_m < 0.1 - 0.3$ ) is caused by inter-grain shading. The shading is attributed to the low surface mobility of adsorbed atoms (adatoms). However, it is likely that the high deposition rate used in Thornton's experiments (100-200 nm/sek) had a considerable influence as well [Zhang and Lagally, 1997].

The gas pressure influences the film structure in this zone in two ways. At high gas pressures, collisions of sputtered atoms with gas atoms are more frequent. The collisions may put the sputtered atoms on an oblique trajectory. This enhances the shadowing effect of growing crystallites. Also, the sputtered atoms can lose a significant fraction of their kinetic energy in collisions with gas atoms. Thus, at low gas pressures, the atoms will transfer more energy to the surface enhancing surface diffusion. As the substrate temperature is increased starting from the zone 1 regime (Fig. 2.6), the energy distribution of the surface atoms first approaches the activation energies of surface diffusion. This enables the filling of the voids and the development of columnar grains. As the substrate temperature is increased further the activation energies of the bulk diffusion are approached resulting in equiaxed grains of increasing size.

Thornton's experiments were not concerned with epitaxial growth. However, his observations do have a certain correlation with film growth on the atomic scale. The mobility of atoms does indeed have a pronounced effect on film growth on the

atomic scale. However, there are a number of mechanisms by which atoms move on a surface, each of which can be described by a rate process [Zhang and Lagally, 1997]. Atomistic rate processes are usually described in terms of the terrace-step-kink (TSK) model illustrated in Fig. 2.8. In addition to terraces, steps and kinks, the figure shows other elemental entities of film growth. These are an adsorbed atom (adatom) and a vacancy on the upper terrace and an island of four atoms on the lower terrace. Let us consider these processes under the preassumption that layer-by-layer growth is thermodynamically feasible. The most important rate process is the diffusion of an adatom on a terrace or flat surface. This process, along with the deposition rate decides the surface mobility. Smooth, uniform films can not be

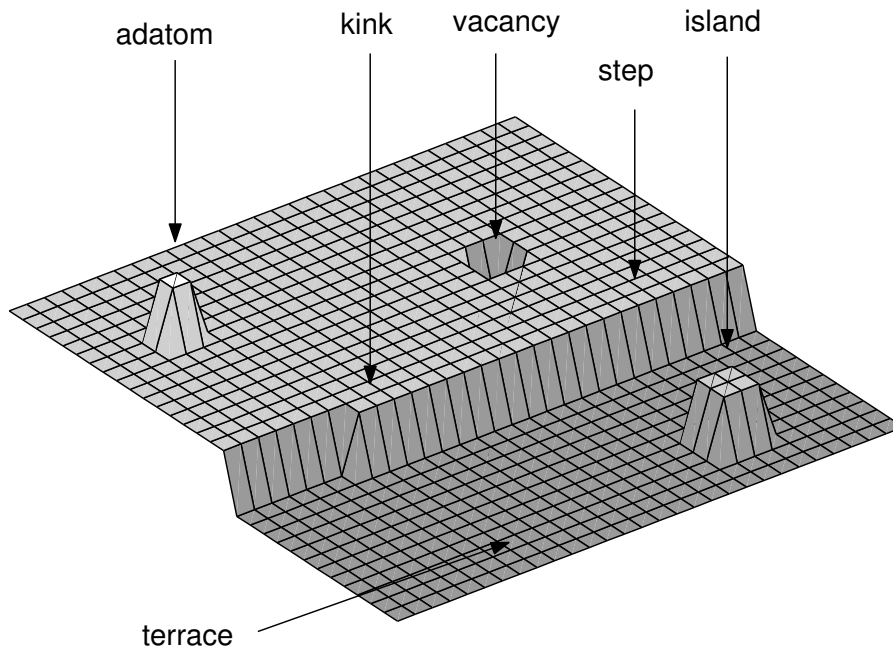


Figure 2.8: The TSK model of a surface for a simple cubic substrate. Each square represents one atom. There are two layers shown. The upper layer only covers roughly half the area shown. The edge of this layer is a step. This step separates the upper and lower terraces. The step has a kink towards the left margin. On the upper terrace is an atom adsorbed on the surface. There is also a site where an atom is missing from the layer, called vacancy. On the lower terrace four adsorbed atoms have formed an island.

formed without sufficient surface mobility. At high deposition rates, a relatively high diffusion coefficient is required for an atom to reach its equilibrium position before it is pinned down by other adsorbed atoms. If the mobility is insufficient the resulting growth front will be rough.

The surface diffusion coefficient is given by

$$D = a^2 k_s \quad (2.3)$$

where  $a$  is the effective hopping distance between sites, and  $k_s \propto \exp(-V_s/k_B T)$  is the site-to-site hopping rate coefficient, where  $V_s$  is the potential-energy barrier between sites,  $T$  is the substrate temperature and  $k_B$  is the Boltzmann constant. At a fixed deposition rate, the value of  $D$  determines the average distance an adatom will have to travel before finding and joining an island. To nucleate an island, enough atoms have to meet to make the total free energy of the island negative. This occurs when the destabilizing positive energy due to the unsaturated bonds of the edge atoms is outweighed by negative cohesive energy between the participating atoms. At sufficiently low temperatures the smallest number of atoms needed to form a stable island is just two atoms. Conversely, increased thermal energy acts as a destabilizing factor. In this context stable does not mean stationary. The island remains mobile as a whole and the atoms can rearrange within the island, diffuse along its edges, and even break away from the island. A stable island is an island that will not decompose completely [Zhang and Lagally, 1997]. At solid surfaces, islands will even remain dynamic indefinitely [Toroczkai and Williams, 1999].

Another prerequisite for a smooth growth front is sufficient interlayer mass transport [Zhang and Lagally, 1997]. While surface diffusion controls the film uniformity in the horizontal direction, interlayer mass transport controls the uniformity in the

vertical direction. The barrier for crossing steps has the biggest influence on inter-layer mass transport. Even if the substrate temperature is high enough to make adatom diffusion along surfaces and island edges possible, hopping off an island to a lower layer may still be difficult. The reason for this is that an adatom has to lower its coordination in order to proceed across the step. Its reluctance to do so is reflected by a higher activation barrier. Therefore, the atom may be trapped on top of the island. This will increase the density of adatoms on top of the island and thus the probability that a new island will be nucleated there prior to the completion of the first layer. Should this effect be predominant, three-dimensional islands will develop and the growth mode will be rough. If this effect is only weak, a stable, smooth growth front can easily be achieved.

This understanding of thin film growth has led to discoveries of various ways to improve thin film quality by manipulating the rate processes during growth. On a small island, an adatom will visit the edges more frequently thereby increasing its chance to hop down. Thus, two-dimensional growth can be enhanced by promoting increased island density and thus lead to smaller islands. By hindering the diffusion along island edges, the island will possess more kinks, and even dendrites. Generally, an atom landing on top of such an island can hop down more easily at a kink site than it would have at a straight step. This kind of manipulation can be achieved with the adjustment of substrate temperature or deposition rate, or by the use of surfactants. Here, the term surfactant refers to impurities added to influence the kinetics, such as diffusion along a step.

## 2.3 Electronic properties at the ultra-thin limit

Physical properties often differ between thin films and the corresponding bulk material. In this section the conductivity of thin metal films will be discussed as well as deviations from the ideal properties of insulators.

### Metal conductivity

The cohesion of solids is entirely provided by electrostatic interactions of the electrons and nuclei [Kittel, 1986, p. 52 - 53]. In metals, the valence electrons are taken away from each atom to form a communal electron sea in which the positive ions are dispersed. These electrons are free to move about, resulting in the high electrical conductivity, which is characteristic of metals. These assumptions form the basis of the Drude model. Many physical properties of metals can be understood in terms of this model [Kittel, 1986, p. 127]. The model was developed long before the invention of quantum mechanics and assisted the derivation of Ohm's law among other things. Later, Fermi-Dirac statistics were applied to the free electrons in a metal providing a consistent description of metallic conduction [Sondheimer, 1952]. According to this model the electrical conductance depends on the number of free electrons per unit volume,  $n$ , and the mean free path (MFP),  $l$  in the following way

$$\sigma_0 = \frac{ne^2l}{m\bar{v}}, \quad (2.4)$$

where  $-e$  is the charge and  $m$  is the mass of an electron, and  $\bar{v}$  is the velocity of an electron at the Fermi surface. The density of free electrons is given by

$$n = \frac{8\pi}{3} \left( \frac{m\bar{v}}{h} \right)^3, \quad (2.5)$$

where  $h$  is Planck's constant. The quantum mechanical analysis of the motion of electrons in a crystal lattice made it possible to give meaning to the two fundamental parameters,  $n$  and  $l$ . The analysis involves a number of energy bands, over which the electrons are distributed. Most of the bands are completely filled, but only the electrons in the remaining unfilled energy bands can participate in electric current conduction. These electrons are the "free electrons" mentioned above. Their density is of the same order as the atomic density. However, their exact density depends on the detailed energy band configuration, and does not necessarily have a simple relation to the atomic density.

In an infinite pure metal at absolute zero temperature, an electron could theoretically move freely without resistance. In practice however, a finite MFP is caused by lattice vibrations, impurities and crystal boundaries. Any of these causes can be predominant in different situations. The MFP due to thermal vibration is a fundamental property of the metal. It is large compared to inter-atomic distances, and increases at low temperatures. A crystal will always contain defects and impurities. Such imperfections cause scattering, and provide an upper limit for the MFP at low temperatures. The third mechanism is surface scattering. When the film thickness is large compared to the MFP, surface scattering will have little influence, because it only affects the current density very close to the surface. When the film thickness approaches the MFP, the influence will increase, resulting in a reduced effective MFP. For this reason thin films have played a central role in the experimental verification of the metallic conduction theory. They provide means of assessing the MFP in terms of the film thickness.

The MFP is associated with a relaxation time,  $\tau$ . If the external forces causing a non-equilibrium energy distribution  $f$  are suddenly removed, the rate at which the

equilibrium distribution  $f_0$  is re-assumed is given by

$$\left[ \frac{\partial f}{\partial t} \right]_{\text{scattering}} = \frac{f - f_0}{\tau}, \quad (2.6)$$

if scattering is the only process of relaxation.

This simple treatment of conduction phenomena remains correct within certain limits. The precise numerical values of the quantities  $m$  and  $n$  have no immediate physical significance. Their values have to be regarded as representing certain averages of the numbers of electrons per unit volume and the effective masses of the electrons in various bands, respectively. However, the detailed theory of the conduction mechanism shows that the results discussed above are a reasonable approximation as far as the electrical conductivity is concerned.

Let us consider a metal slab, to which a voltage is applied [Sondheimer, 1952]. The resulting electric field produces a force on the electrons. If we equate the rate of change in the electron energy distribution,  $f$ , due to the electric field to the rate of change due to scattering mechanisms according to Eq. (2.6), the steady-state result will be

$$-\frac{e}{m} \mathcal{E} \cdot \nabla_{\mathbf{v}} f = -\frac{f - f_0}{\tau}, \quad (2.7)$$

where the equilibrium distribution  $f_0$  is the Fermi-Dirac distribution function. This is the Boltzmann equation for quasi-free electrons. After solving Eq. (2.7), the current density may be calculated

$$\mathbf{J} = -2e \left( \frac{m}{h} \right)^3 \int \mathbf{v} f d\mathbf{v}. \quad (2.8)$$

Although the theory presented here has been criticized for not being entirely rigorous from a quantum mechanical point of view, it has had great success in

explaining experimental facts. It has been shown to be directly applicable to the monovalent alkali metals, and to provide a qualitative picture of more complex metals, indicating a correct order of magnitude. This strongly supports the basic validity of its assumptions [Sondheimer, 1952]. This theory has been applied to the analysis of conduction in thin films [Sondheimer, 1952, Fuchs, 1938]. Fig. 2.9 illustrates a metal film of thickness  $a$ . The film surfaces are the planes  $z = 0$  and  $z = a$ . This is a one-dimensional problem, so the distribution function can be written

$$f = f_0 + f_1(\mathbf{v}, z), \quad (2.9)$$

where the function  $f_1$  has to be determined. An electric field is applied in the  $x$ -direction. Then equation (2.7) becomes

$$\frac{\partial f_1}{\partial z} + \frac{f_1}{\tau v_z} = \frac{e\mathcal{E}}{mv_z} \frac{\partial f_0}{\partial v_x}. \quad (2.10)$$

Finding a general solution to this equation is straightforward. The exact solution follows as boundary conditions are introduced. In the simplest case, it may be assumed that every free path is terminated by a collision at the surface, so that the

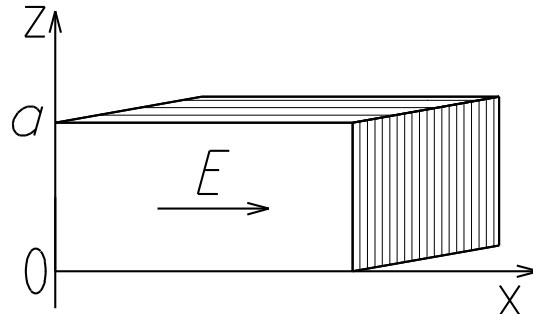


Figure 2.9: A metal film of thickness  $a$ . The film surfaces are the planes  $z = 0$  and  $z = a$ , and the electric field,  $\mathcal{E}$  is parallel to the  $x$ -axis.

scattering is purely diffuse. Solving Eq. (2.10) with these boundary conditions and combining the result with Eqs. (2.8) and (2.9) gives the current density

$$J(z) = \frac{4\pi e^2 m^2 \tau \bar{v}^3}{h^3} \mathcal{E} \int_0^{\pi/2} \sin^3 \theta \left( 1 - \exp \left[ -\frac{a}{2/\cos \theta} \right] \cosh \left[ \frac{a-2z}{a/\cos \theta} \right] \right) d\theta \quad (2.11)$$

across the thickness of the film, where  $l = \tau \bar{v}$  is the mean free path of the electrons at the surface of the Fermi-Dirac distribution. By integrating the current density over  $0 \leq z \leq a$ , the ratio of the effective resistivity,  $1/\sigma$ , to the bulk resistivity,  $1/\sigma_0$ , may be found. The limiting form for thick films is given by

$$\frac{\sigma_0}{\sigma} = 1 + \frac{3}{8\kappa}, \quad \kappa \gg 1, \quad (2.12)$$

where  $\kappa = a/l$ . For very thin films we have

$$\frac{\sigma_0}{\sigma} = \frac{4}{3\kappa \log(1/\kappa)}, \quad \kappa \ll 1. \quad (2.13)$$

It is by no means certain that all the electrons are diffusely scattered from the surface, some may be specularly scattered. This can be translated to the boundary conditions by letting the velocity of scattered electrons be conserved, for a fraction  $p$  of the scattered electrons, only reversing the vertical component. In that case, the limiting form for thick films is given by

$$\frac{\sigma_0}{\sigma} = 1 + \frac{3}{8\kappa}(1-p), \quad \kappa \gg 1, \quad (2.14)$$

and for very thin films we have

$$\frac{\sigma_0}{\sigma} = \frac{4}{3} \frac{1-p}{1+p} \frac{1}{\kappa \log(1/\kappa)}, \quad \kappa \ll 1. \quad (2.15)$$

A further improvement of the model can be made by including the effects of surface roughness [Namba, 1970]. Although rough surfaces commonly have a very complicated topography, it can generally be regarded as consisting of gentle undulations with superposed irregular indentations. It has been suggested that the irregular indentations be included in the specularity parameter  $p$  described above, and the undulations be accounted for as a sinusoidal variation in the film thickness.

$$a'(x) = a + h \sin \left( n \frac{2\pi}{L} x \right), \quad (2.16)$$

where  $h$  is the amplitude of the sinusoidal roughness,  $L$  is the length of the film, and  $n \frac{2\pi}{L}$  is the wavelength of the undulations. This way the ratio of the effective film resistivity to the bulk resistivity is given by an integral over  $x$

$$\frac{\sigma_0}{\sigma} = \frac{\kappa}{L/\sigma_0} \int_0^L \sigma(a'(x)) \left[ \kappa + \frac{h}{l} \sin \left( n \frac{2\pi}{L} x \right) \right] dx, \quad (2.17)$$

It can be seen from Eq. (2.17), that roughness increases the resistivity. Thus, it may be concluded that in order to minimize the resistivity of a ultra-thin metal film, the roughness should be as small as possible, and imperfections such as crystal defects and impurities should be avoided.

### Insulators

The band diagram of a metal-insulator-metal (MIM) structure is shown in Fig. 2.10. The diagram suggests a perfect insulator, i.e. that electrons are unable to get from one side to the other because there are no suitable energy levels allowed within the insulator. However, for high electric fields, reduced thickness or imperfect material, the insulator performance may be affected.

It has been reported for wide bandgap materials that the band structure may

be strongly modified at nanometer lengthscales [Alivisatos, 1996]. This is in agreement with reports on  $\text{Al}_2\text{O}_3$  [Murata et al., 2001b], where the bandgap was observed to reduce with reduced thickness. At 3 nm the bandgap was close to the bulk value of 9 eV, and decreased to 3 eV for 0.3 nm thick films. However, it has been demonstrated for MgO grown on Ag [Schintke et al., 2001, Kiguchi et al., 2002] that smooth epitaxial films grown in a layer-by-layer fashion maintain the bandgap value of the corresponding bulk surface down to a few monolayers. This has been observed for films as thin as a single monolayer [Kiguchi et al., 2002]. The surface bandgap is usually only a few electron volts lower than the bulk bandgap. For MgO it is approximately 6 eV, as compared to the bulk bandgap is 7.8 eV [Schintke et al., 2001, Kiguchi et al., 2002].

Another deviation from ideal properties of insulators is the nonzero current density through the insulator [Hori, 1997, p. 44 - 47]. Typical conduction processes are illustrated in Fig. 2.11. Let us first look at conductance not related to impurities or structural imperfections. A simple model of the MIM structure conductance is given by a current of free particles which encounter a finite potential step

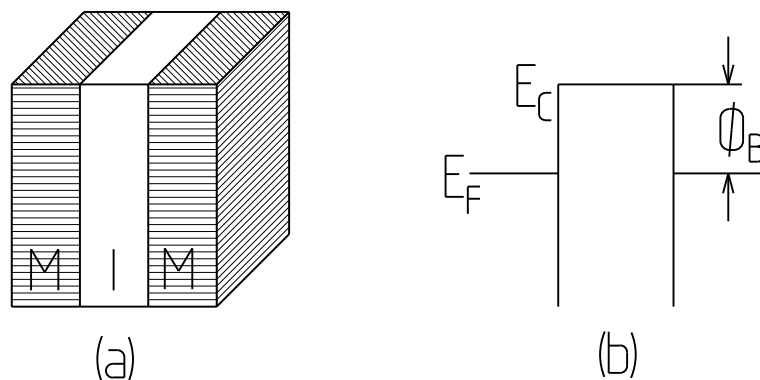


Figure 2.10: (a) The physical structure, and (b) band diagram of a metal-insulator-metal (MIM) system.

[Davies and Betts, 1994, 47 - 51]. Even though the energy of the particles is lower than the potential step, their wavefunction does not vanish at the step, but falls off exponentially into the step. In the case of the MIM structure, this means that there is a finite probability that electrons from either of the metal layers can travel a short distance into the insulator despite the lack of allowed energy levels there. The overlapping of the wavefunctions gives rise to the direct tunneling current density [Muller et al., 1999], given by [Hori, 1997, p. 45]

$$J_{\text{DT}} = \frac{q^2}{2\pi\hbar d^2} \left\{ (\phi_{\text{B}} - \frac{V}{2}) \exp \left[ -\frac{4\pi d}{h} (2m_e^* q)^{1/2} (\phi_{\text{B}} - \frac{V}{2})^{1/2} \right] - (\phi_{\text{B}} + \frac{V}{2}) \exp \left[ -\frac{4\pi d}{h} (2m_e^* q)^{1/2} (\phi_{\text{B}} + \frac{V}{2})^{1/2} \right] \right\}, \quad (2.18)$$

where  $q$  is the electron charge,  $h$  is Planck's constant,  $\phi_{\text{B}}$  is the tunneling barrier height,  $V$  is the applied voltage,  $d$  is the insulator thickness, and  $m_e^*$  is the effective mass of an electron. The direct tunneling process is illustrated in Fig. 2.11 (a). The degree of wavefunction overlapping strongly depends on the thickness, and so does the tunneling current. This has been verified experimentally for a metal-oxide-semiconductor structure [Muller et al., 1999]. Using atomic-scale electron-energy-loss-spectroscopy, energy levels aligned with the semiconductor conduction band were found in the insulator conduction band. These correspond to the decaying wavefunctions. A correlation between the tunneling current density and the spatial

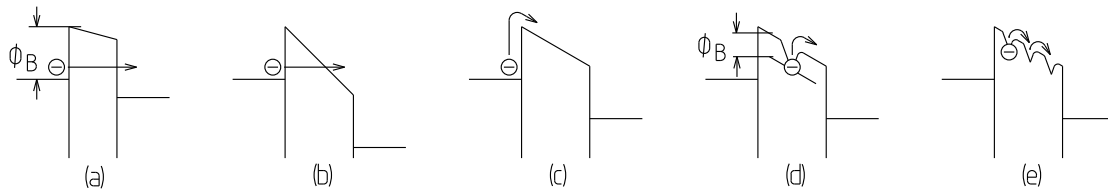


Figure 2.11: Typical conduction processes in a metal-insulator-metal structure: (a) Direct tunneling, (b) Fowler-Nordheim tunneling, (c) Thermionic emission, (d) Poole-Frenkel emission, and (e) ohmic hopping conduction.

separation of the states belonging to the two interfaces was also reported. For relatively thick films direct tunneling will not occur.

If an increasing voltage is applied to the MIM structure, the far end of the insulator conduction band eventually reaches the Fermi energy of the metal. Beyond that point electrons will be able to tunnel into the insulator conduction band. This is called Fowler-Nordheim (FN) tunneling and is illustrated in Fig. 2.11 (b). The FN tunneling current density is given by [Hori, 1997, p. 45]

$$J_{\text{FN}} = \frac{q^2}{8\pi h \phi_{\text{B}}} \mathcal{E}^2 \exp \left[ -\frac{8\pi \sqrt{2m^*} q \phi_{\text{B}}^{3/2}}{3h\mathcal{E}} \right], \quad (2.19)$$

where  $\mathcal{E}$  is the electric field across the insulator. Thus  $\ln(J/\mathcal{E}^2)$  versus  $1/\mathcal{E}$  will produce a straight line, the slope of which will give the barrier height  $\phi_{\text{B}}$ . The effective thickness for this field assisted tunneling decreases as the field is further increased. This is reflected in the high electric field dependency of the current density in Eq. (2.19). The insulator conduction band edge will coincide with the Fermi level in the metal for  $\mathcal{E}d = \phi_{\text{B}}$ . This provides a simple criterion that FN tunneling occurs rather than direct tunneling when

$$V \equiv \mathcal{E}d > \phi_{\text{B}}. \quad (2.20)$$

The transition from direct tunneling to FN tunneling can be seen in Fig. 2.12, where the thickness and electric field dependence of intrinsic conduction processes is illustrated. If FN tunneling is the predominant process, the conduction can be suppressed by lowering the voltage. On the other hand, if direct tunneling is the predominant process, lowering the voltage will not be as successful because the voltage dependence is much weaker.

The energy distribution of electrons within a solid is given by the Fermi-Dirac

distribution function. This means that at elevated temperatures, an increasing fraction of the electrons in the metal will have energy surpassing the potential step presented by the insulator energy gap. They can travel across the insulator, as illustrated in Fig. 2.11 (c), resulting in a current density

$$J_{TE} \propto T^2 \exp\left(-\frac{\phi_B - \sqrt{\mathcal{E}q/4\pi\epsilon}}{k_B T}\right), \quad (2.21)$$

where  $k_B$  is the Boltzmann constant. This is called thermionic emission. The density of high energy electrons increases with increasing temperature according to the Fermi-Dirac distribution function, thus the strong temperature dependence of  $J_{SE}$ .

Let us now turn to the conduction processes that are caused by structural imperfection. During the preparation of insulating layers, defects may be generated, e.g.

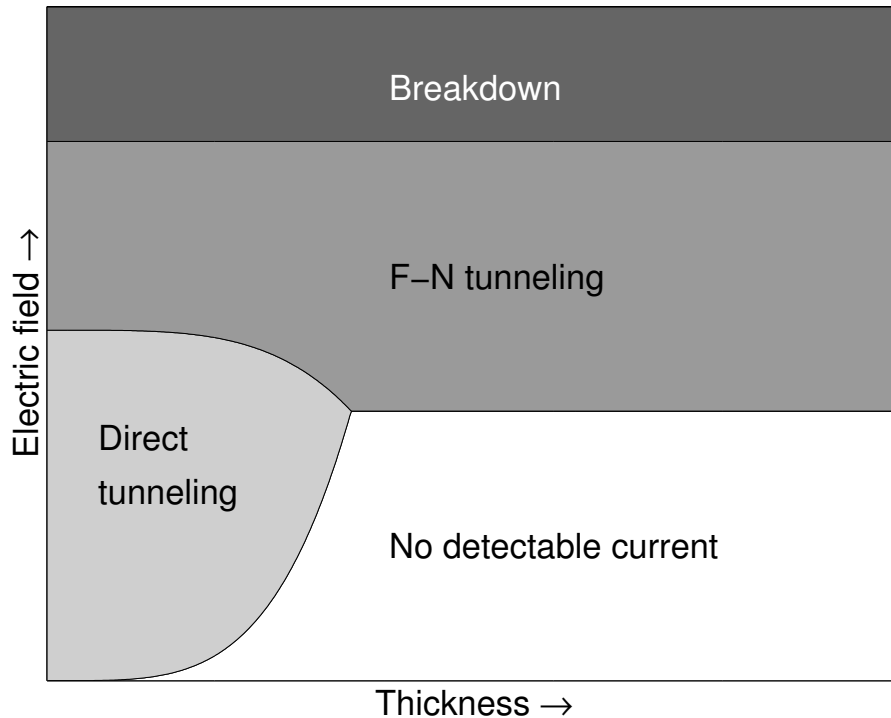


Figure 2.12: Diagram illustrating the thickness and electric field dependence of intrinsic conduction process occurrence (adapted from [Hori, 1997, p. 45]).

due to dislocations or impurity atoms. These defects can act as electron traps, i.e. due to broken bonds or different valence of impurity atoms they can accommodate an electron [Hori, 1997, p. 162 - 164]. Field-enhanced thermal excitation of the trapped electrons into the conduction band can make a contribution to the current density [Hori, 1997, p. 44 - 46]

$$J_{\text{PF}} \propto \mathcal{E} \exp\left(-\frac{\phi_{\text{B}} - \sqrt{\mathcal{E}q/4\pi\epsilon}}{k_{\text{B}}T}\right), \quad (2.22)$$

where  $\phi_{\text{B}}$  is the trap barrier height as illustrated in Fig. 2.11 (d). This process is called Poole-Frenkel (PF) emission, and is thermally activated. Thus, it will subside at low temperatures.

At elevated temperature, ohmic conduction due to thermally excited electrons hopping from one isolated state to the next becomes possible, as illustrated in Fig. 2.11 (e), giving rise to a current density

$$J_{\text{HC}} \propto \mathcal{E} \exp\left(-\frac{\Delta E_{\text{ae}}}{k_{\text{B}}T}\right), \quad (2.23)$$

where  $\Delta E_{\text{ae}}$  is the electron activation energy. This type of conduction is only observed if the insulator is contaminated with impurities.

The insulator leakage current itself is not the only concern. Under high-field stress, insulating films will eventually reach breakdown [Hori, 1997, p. 172 - 188]. The breakdown event usually causes irreversible damage leading to increased leakage current and eventually fatal device failure. For each material there is a critical electric field, at which breakdown will occur. The physical meaning of breakdown is the destruction of the atomic structure by breaking inter-atomic bonds. Various imperfections can cause an insulating material to break down at a lower voltage than anticipated. Such events are usually related to charge buildup for some reason,

which locally increases the electric field.

Breakdown has been studied extensively for the metal-SiO<sub>2</sub>-Si system, because of its importance in integrated circuit manufacturing. The properties of this system can provide a general understanding of insulator reliability although it may be fundamentally different from other practical systems as will be discussed below. There are three distinct types of breakdown [Hori, 1997, p. 172 - 188]. Firstly, there are films which originally have a defect shorting the insulator immediately causing conduction at low fields (Mode A). Secondly, there are films which contain a weak spot originally not conductive (Mode B). The weak spot may be due to localized thin regions or asperities resulting in a locally increased electric field, which causes premature breakdown. Other reasons may be reduced barrier height or increased trap generation rate, due to organic or inorganic particle contamination, or substrate defects such as stacking faults, and oxygen or carbon precipitates. Both tunneling electrons and carriers created by impact ionization can be caught by traps. Furthermore, impact ionization at a defect site can generate new carrier traps, especially in the presence of strain. Charged traps may locally add to or reduce the electric field, depending on their spatial position. If they add to the electric field, tunneling current density will increase. The tunneling current will accelerate trap charging and increase the trap generation rate. Breakdown modes A and B are both influenced by structural variations and impurities and are therefore called extrinsic breakdown modes. The third type of breakdown is intrinsic breakdown (Mode C). Intrinsic breakdown means that the insulator film will exhibit the full breakdown strength of the bulk material. This can only be achieved with a defect-free sample, which of course does not exist. In practice this mode is achieved when the defects are small enough not to trigger breakdown until approximately at the critical field.

There are a number of important differences between SiO<sub>2</sub> applied in MOSFETs

and insulating films epitaxially grown on suitable substrates. Thermal SiO<sub>2</sub>, commonly used in integrated circuit manufacturing, is amorphous [Hori, 1997, p. 149] and contains micro-pores and voids [Hori, 1997, p. 175]. This lowers the intrinsic breakdown strength and is one of the sources of the carrier traps mentioned above. In dense crystalline films these problems are presumably not present. In particular, carrier trap density can be expected to be negligible. Furthermore the complex process of integrated circuit fabrication requires cleaning and etching steps which leave organic and inorganic particles behind [Hilleringmann, 1999, p. 150 - 159]. Also the processing takes place in a clean room, which contains a finite density of dust particles, although low.

The breakdown characteristics are also affected by the system structure. The choice of electrode material can have a negative influence [Hori, 1997, p. 186 - 187]. If the reactivity between the electrode and the insulator materials is strong, breakdown will occur sooner. This effect is stronger for thinner films. On the other hand, increased breakdown strength has been observed for ultra-thin oxides compared to thicker oxides [Hori, 1997, p. 184 - 185]. This is believed to be due to a reduction in impact ionization at reduced thickness.

Depending on the application, an epitaxial MIM structure may possibly be formed entirely in a vacuum environment without any steps involving wet chemicals. The required patterns could then be defined and etched afterwards. That way the delicate metal/insulator interfaces will not be affected. With proper substrate cleaning and annealing prior to growth, all contamination sources listed above could practically be eliminated. This leaves only two possible sources of premature breakdown: localized thin regions and asperities. Both breakdown sources can be minimized by effectively controlling the roughness.

### **Metal-insulator stacks**

The most important requirements for achieving functional ultra-thin metal-insulator stacks can therefore be summarized as the following. The two materials must be chosen so that the formation of a surface of each material is thermodynamically feasible on the other. This means that their respective surface energies have to be similar and a certain degree of chemical interaction has to be present. Under these circumstances two-dimensional growth may be achieved, which minimizes the interface roughness. The chemical interaction can not be too strong. That would affect the breakdown strength and cause alloying at elevated temperatures. The two materials also have to have compatible crystal structures. The film strain should not exceed a few percent. This is the main prerequisite for heteroepitaxy, and also eliminates interface defects due to unsaturated bonds. The substrate has to be as close to atomic smoothness as possible. That can be achieved by either annealing or homoepitaxy prior to film growth as discussed in the following chapter. It is also possible to choose a third material as a substrate. In that case the substrate must be lattice matched to both the film materials and have a suitable surface energy.

# Chapter 3

## Materials for ultra-thin films

The importance of the correct choice of materials for the construction of smooth nanoscale stacks was discussed in the previous chapter. There is a large body of work concerned with the physical and chemical properties of ultra-thin films. There are however many unexplained features in ultra-thin film growth, and thus ultra-thin films are only occasionally found in an industrial manufacturing setting. The best known example of ultra-thin film applications is probably the gate dielectric in ultra-large-scale-integration (ULSI) MOSFETs. Its properties have been documented extensively [Hori, 1997]. However, that knowledge is highly specific for the case of thermally oxidized silicon, and thus, it can not entirely be transferred to other systems, as was discussed in section 2.3. Also the goal in MOSFET gate dielectric design is to maximize the capacitance without causing too much increase in the tunneling current, whereas the aim of this work is to minimize the tunneling current, while keeping the capacitance as low as possible. Other applications of metal/insulator heterostructures include magneto-tunneling junctions, resonant tunneling diodes, X-Ray mirrors and model systems for surface science research. This chapter will survey recent work on ultra-thin films, film stacks and superlattices.

### 3.1 Metals on insulating substrates

The thickness dependent resistivity of ultra-thin Cu films has been explored for the purpose of assessing the lower limit of their thickness for use as interconnects in integrated circuits [Liu et al., 2001]. It was found that grown on amorphous SiO<sub>2</sub> ultra-thin Cu films consisted of isolated islands. At a thickness of about 10 nm the sheet resistance of the films was observed to drop rapidly indicating the formation a continuous film. It has been found that the application of filtered cathodic arc deposition instead of magnetron sputtering for growing Ag films on ZnO coated glass resulted in a reduction in the minimum film thickness for film coalescence from 8 to 6 nm [Byon et al., 2003]. In the cathodic arc system, film-forming atoms arrive at the substrate with hyper-thermal energies (10 - 100 eV). The results clearly indicate the influence of incident particle energy on thin film growth. However, the films were thermodynamically unstable, and exhibited aging on a time-scale of minutes. Pt films on MgO have been characterized structurally [Menendez et al., 1998] in order to provide a basis for studying their physical properties. Despite the relatively large lattice mismatch of Pt to MgO it forms smooth films of good crystalline quality at low temperatures. At higher temperatures, however, the lattice mismatch results in drastic changes towards three-dimensional island growth. The authors attribute the low growth temperature required for smooth films to the energetic particles of the magnetron sputtering process used.

The effects of discharge parameters on the properties of thin Pt and Al films deposited in a RF magnetron sputtering discharge have been studied [Kawamura et al., 2000]. For films grown on glass, where there is no crystallographic preference, it was found that Pt grew in a layer-by-layer mode, while aluminum grew in a three-dimensional island mode. The coalescence thickness of Pt was between 0.4 and 1 nm, and did not strongly depend on any of the parameters. However, Al behaved very differ-

ently. Al films ranged from 1 to 9 nm in coalescence thickness, the higher values being associated with increased substrate temperature and greater target-substrate distance.

## 3.2 Crystalline insulators on metal substrates

There has been some success in growing single-crystal insulators on metal substrates. The main objectives have been to obtain a better understanding of surface and interface properties and to analyze the catalytic effect of metals.

### Silicon Dioxide

Silicon dioxide is exclusively used in its amorphous form in microelectronic applications as discussed above. However, it also has a number of different crystalline variations. Thin single-crystalline silicon dioxide films have been grown on a Mo(112) substrate [Schroeder et al., 2001]. Molybdenum has an fcc crystal structure [Gray, 1972] but the group noted that the (112) surface presents a nearly hexagonal symmetry which triggers the growth of crystalline silicon dioxide [Schroeder et al., 2001]. They concluded that it was the (0001) face of  $\beta$ -tridymite  $\text{SiO}_2$  which has a hexagonal structure. The films ranged from 0.5 to 0.8 nm in thickness. The films were deposited by repeated cycles of deposition and oxidation. A small amount of silicon was evaporated each time by electron bombardment of a Si rod. The resulting film was subsequently oxidized. The ordered crystal only appeared after an elaborate annealing procedure. The films proved to be continuous.

Single-crystal  $\alpha$ -quartz  $\text{SiO}_2$  films, have also been grown on Ni(111) substrate [Kundu and Murata, 2002]. The films had a  $(\sqrt{3} \times \sqrt{3}) R30^\circ$  crystallographic orientation. The lattice constant along this surface is approximately double that of the

Ni(111) surface. The film was prepared by depositing a roughly 3 nm thick Si film at room temperature by thermal evaporation from a Si wafer. This was followed by oxidation in the presence of atomic hydrogen at an increased temperature (350°C). Finally, the sample was annealed at 800°C in an O<sub>2</sub> atmosphere also in the presence of atomic hydrogen. In the absence of either O<sub>2</sub> or atomic hydrogen the film did not crystallize. The authors suggest that the hydrogen acts as a network modifier opening the fully connected (SiO<sub>4</sub>)-tetrahedral network in the amorphous oxide film. The process described above resulted in an oxide of 4 nm thickness. The group had no success in growing thinner films. Instead a nickel-silicide film was formed. They conclude that the growth mechanism is quite different from that described by Schroeder et al. [Schroeder et al., 2001] above.

### **Aluminium Oxide**

Single-crystal  $\alpha$ -Al<sub>2</sub>O<sub>3</sub>, 0.5 - 3 nm thick, have been grown on Ru(0001), using the phase transition of an as-grown amorphous oxide film [Murata et al., 2001b]. The lattice mismatch of  $\alpha$ -Al<sub>2</sub>O<sub>3</sub> to Ru(0001) is small and the melting point of Ru is much higher than the transition temperature from  $\gamma$ - to  $\alpha$ -Al<sub>2</sub>O<sub>3</sub>. The film was grown by depositing Al from a tungsten basket on the Ru surface followed by oxidation in an O<sub>2</sub> atmosphere. The authors note that the deposited Al should be less than 1 nm thick. For thicker films the oxidation becomes problematic. After annealing a LEED (Low Electron Energy Diffraction) pattern indicating single crystalline Al<sub>2</sub>O<sub>3</sub> appeared. The formation of a well structured film was confirmed with a scanning-tunneling-microscope (STM). The thickness of the oxide film was estimated to be 0.9 nm for a 1 nm deposited Al layer and the authors note that thinner films were easily fabricated by controlling the thickness of the Al film. The film was shown to be a single domain over a region larger than 0.1 x 0.1  $\mu\text{m}^2$ . An interesting

result presented by the group was the insulator band gap dependence on the oxide thickness. At 3 nm the band gap of the oxide layer was nearly equal to the bulk band gap of 9 eV but was estimated to be approximately 3 eV at 0.9 nm. The same group then fabricated Pt monolayers on 1 nm thick  $\alpha$ -Al<sub>2</sub>O<sub>3</sub> by evaporation [Murata et al., 2001a]. The formation of a Pt monolayer was verified by scanning tunneling microscope (STM). The Pt overlayer exhibited a disordered structure.  $I - V$  measurements showed constant resistivity, i.e. metallic characteristics. The  $I - V$  measurements taken at the bare oxide on the other hand showed a clear flat region, i.e. insulating characteristics.

### Magnesium Oxide

A comparative study of MgO thin films prepared on Ag(001) by two different procedures has been made [Valeri et al., 2001]. The films were grown by molecular beam epitaxy (MBE) and by DC sputtering, respectively. In the case of MBE growth, Mg was evaporated in an O<sub>2</sub> atmosphere. For growth by DC sputtering a composite MgO target was bombarded with 3 keV Ar<sup>+</sup> ions, and no reactive gas was used. In both cases, the films were grown at a substrate temperature of 190°C. It was found that the different deposition methods resulted in films with similar stoichiometry, morphology and structure. At low thickness the strain is considerable because of the lattice mismatch. It was reported that films grown by sputtering had formed a relaxed structure at a lower thickness than the films grown by MBE (8 vs. 10 monolayers (ML)). Furthermore, different growth modes were observed for the two different growth procedures. Films prepared by MBE grew in a layer-by-layer fashion, while sputter deposited films formed islands which only coalesced as the thickness approached 10 ML. The group further investigated the initial growth regime (0.25 - 1.25 ML) for deposition by MBE [Valeri et al., 2002a]. They performed a detailed

quantitative investigation of the evolution of the MgO/Ag(001) interface morphology as a function of thickness using a scanning tunneling microscope (STM). The substrates used consisted of large terraces separated by monoatomic steps. As the reactive MBE deposition proceeded surface disruption was observed. This involved the removal of Ag atoms from the substrate forming islands and leaving vacancies behind. MgO grew on the terraces, islands and in the vacancies. At 1 ML nominal deposition the substrate fractional coverage was observed to be 85%, with a relevant number of three-dimensional pyramidal islands present. Finally the group examined the thickness dependence of the strain in MgO films deposited on Ag(001) by MBE [Valeri et al., 2002b]. They observed strain accommodation by tetragonal distortion. At 3 ML they observed 3.6% tensile strain along the growth axis and 3.1% compressive strain in the growth plane. The strain was observed to relax as the films reached a critical thickness of about 9 ML. They noted that an almost complete substrate coverage was obtained for 3 ML nominal thickness.

MgO films have been grown on Ag(100) by evaporation from an Mg rod. A comparative study of oxidation during and after growth, respectively, was performed [Wollschlager et al., 1999]. It was found that films oxidized during deposition grew epitaxially with a single orientation. The post-deposition oxidized films, however, proved to have rotational grains. This was attributed to the way MgO (fcc) islands nucleate on Mg (hcp). MgO forms islands aligned with the atomic rows of Mg. Thus the islands can have three different orientations in the growth plane, each rotated by  $120^\circ$ .

Kiguchi et al. investigated the heteroepitaxial growth of MgO on Ag(001) [Kiguchi et al., 2002]. They prepared high-quality films by evaporating MgO with electron-beam evaporators at a substrate temperature of 450K. With Electron Energy Loss Spectroscopy (EELS) they observed a constant band gap energy of ap-

proximately 6 eV from 1 to 20 monolayers.

A number of studies involving MgO growth on Si and GaAs have been made. The purpose is to develop buffer layers which allow the growth of epitaxial superconducting, ferroelectric and ferromagnetic films on semiconducting substrates while avoiding the problems caused by the lattice mismatch and chemical reactivity [Stampe and Kennedy, 1998]. The method of substrate preparation has been reported to influence the growth orientation on these substrate. A systematic investigation of reactive gas pressure influence on the properties of MgO films deposited on Si in a pulsed mid-frequency magnetron sputtering discharge has been made [Cheng et al., 2002, Cheng et al., 2003]. At low oxygen flow rate (3 sccm) the film orientation was mainly MgO(200), with a visible MgO(220) Bragg peak. As the flow rate was increased, the MgO(220) peak quickly grew stronger, and soon became dominant. At the same time, a considerable decrease in mosaic thickness was observed, and a decrease in the film surface roughness. MgO deposition on Si and GaAs by laser ablation of Mg in an O<sub>2</sub> atmosphere has been explored [Stampe and Kennedy, 1998]. High quality crystalline films were achieved in both cases. The optimum growth temperature was found to be 500°C for Si, and 350°C for GaAs.

For reactive RF magnetron sputtering deposition of MgO films on Si, a comparison of the use of an Mg and sintered MgO target has been made, respectively [Caceres et al., 2002]. In both cases crystalline films were achieved, the greatest intensity of the diffraction peak was observed for an oxygen-to-argon proportion of 20%. However, the films did not have the same crystal structure. The films deposited from an Mg target had an MgO rocksalt structure, while the films deposited from an MgO target contained Mg(OH)<sub>2</sub> and had a cubic spinel structure. The presence of OH was confirmed with X-Ray photoelectron spectroscopy (XPS). Due

to the lower sputtering yield of MgO, the deposition rate was two times greater for the Mg target.

### 3.3 Metal-insulator heterostructures

Lattice mismatch between film and substrate, or between layers in a stack, causes strain in the film. Strain increases the free energy of the interface which can induce island formation and thus increased roughness, and possibly a greater minimal thickness for film continuity. The roughness in turn increases the resistivity of ultra-thin films [Namba, 1970], and the risk of insulator breakdown [Hori, 1997, p. 172 - 188]. Also films can develop dislocations to relax strain. These dislocations further degrade the film properties. Heterostructure materials are usually chosen in such a way that their crystal structures are compatible. It has been suggested [Kado et al., 1999, Kado, 1996, Chambers et al., 1995] that by using metal alloys, the lattice constant may be adjusted to a value that closely matches the film to the lattice constants of other materials in the system. Thereby the odds of achieving the desired two-dimensional, or layer-by-layer growth are increased. For the widely used substrate MgO two different alloys have been proposed. Kado et al. [Kado et al., 1999, Kado, 1996] constructed a superlattice of MgO and a Ti-Ag alloy on an MgO substrate for application in ultra-high speed electronic devices. They characterized the system structurally and concluded that using a lattice-matched alloy instead of elemental metal resulted in improved epitaxy and crystal quality. Chambers et al. [Chambers et al., 1995] used a Cr-Mo alloy with MgO. They realized an  $\text{MgO}/\text{Cr}_x\text{Mo}_{1-x}/\text{MgO}(0\ 0\ 1)$  structure using molecular beam epitaxy (MBE). They reported that the binary metal alloy film had good crystal quality and grew in a layer-by-layer fashion.

Pt/ $\text{Al}_2\text{O}_3$  superlattices with a layer period of 7 nm have been prepared by sputtering on the (11 $\bar{2}$ 0) plane of  $\text{Al}_2\text{O}_3$  [Morawe and Zabel, 1995]. They report that sputter deposited platinum films are polycrystalline with interface roughness less than 0.2 nm. Upon annealing at 700 – 800°C the crystal grains align epitaxially parallel to the substrate lattice. The formation of a superlattice in the multi-layer structure was confirmed with X-Ray diffraction.

### 3.4 The $\text{Cr}_x\text{Mo}_{1-x}/\text{MgO}$ system

In the current study we chose the  $\text{Cr}_x\text{Mo}_{1-x}/\text{MgO}$  system for further investigation. The Chromium-Molybdenum alloy has been suggested as a good match to the commonly used substrate material MgO as discussed above. The two metals are both quite close to being lattice matched to MgO, Mo having a slightly smaller and Cr having a slightly larger lattice constant, respectively, as can be seen in Table 3.1. The alloy lattice constant scales linearly with the composition allowing a better than 99% match for proportions  $\text{Cr}_x\text{Mo}_{1-x}$  in the range  $0.56 \leq x \leq 0.80$ . Additionally, the Cr-Mo alloy has the advantage that its surface free energy for the lattice-matched composition is very close to that of MgO as discussed below, thus increasing the probability that the construction of a stack of the two materials may be possible. Furthermore, both the materials have relatively low chemical reactivity and are thus likely to be stable in a variety of settings.

#### The MgO substrate

MgO is a widely used substrate for epitaxial growth of metals [Rickart et al., 2001]. This is because of its low cost, high temperature stability and low chemical reactivity. Furthermore its lattice mismatch to various metals is only slight, as shown in Table

	lattice	$a$ [nm]	$d_{\langle 011 \rangle}$ [nm]	strain[%]
<b>Ag</b>	fcc	0.4086		3.01
<b>Au</b>	fcc	0.4078		3.20
<b>Al</b>	fcc	0.4050		3.87
<b>Pd</b>	fcc	0.3891		7.64
<b>Pt</b>	fcc	0.3924		6.86
<b>Cr</b>	bcc	0.2885	0.4079	3.18
<b>Fe</b>	bcc	0.2866	0.4054	3.77
<b>Mo</b>	bcc	0.3147	0.4451	-5.65

Table 3.1: The first column shows the lattice type of chosen metals. The second column shows the lattice constants,  $a$ , of the metals. The third column shows the inter-atomic distance along the  $\langle 011 \rangle$  direction for bcc metals. The last column shows the strain obtained for epitaxial growth on MgO(001) ( $a_{\text{MgO}} = 0.4213$  nm). Positive strain indicates tensile stress, whereas negative strain indicates compressive stress. For fcc metals the epitaxial relationship is assumed to be  $\langle 001 \rangle \parallel \langle 001 \rangle$  and for bcc metals the relationship is assumed to be  $\langle 001 \rangle \parallel \langle 011 \rangle$ .

3.1, where the properties of several metals are displayed. The first column of the table shows the lattice type of the metals, and the second column shows the lattice constants. The third column shows the inter-atomic distance along the  $\langle 011 \rangle$  direction for those metals that have a bcc crystal structure. The last column shows the strain obtained for epitaxial growth on MgO(001). Positive strain indicates tensile stress, whereas negative strain indicates compressive stress. For fcc metals the epitaxial relationship is assumed to be  $\langle 001 \rangle \parallel \langle 001 \rangle$  and for bcc metals the relationship is assumed to be  $\langle 001 \rangle \parallel \langle 011 \rangle$ .

The chemical structure and morphology of the substrate surface dramatically influence film quality. Rickart et al. [Rickart et al., 2001] examined the effect of MgO substrate carbon contamination on thin Ag and Au layers (150 nm), which they use as buffer layers for Fe films. They developed a technique for preparing carbon-free MgO surfaces. They use a low-energy (10-100 eV) oxygen ion beam generated by electron cyclotron resonance wave (ECRW) controlled plasma reactor. While substrates cleaned by conventional methods of rinsing and annealing in UHV at 600°C

for 180 minutes revealed an effective carbon coverage of 0.17 monolayers (ML) as evaluated by Auger electron spectroscopy (AES), substrates prepared by the oxygen ion beam method did not demonstrate any traces of carbon within the detection limit of 0.01 ML. These substrates also exhibited an improved surface roughness of about 0.1 nm as compared to 0.7 nm for substrates before annealing. Homoepitaxial growth is another way of eliminating surface contamination and roughness. In that case, the FM growth condition presented in equation (2.2) is rigorously fulfilled. During monolayer-by-monolayer growth the surface gradually becomes smoother, and any surface contaminants will be buried deep under the surface. This has been proven to be effective for MgO [Chambers et al., 1994]. Both of the above mentioned methods are performed in vacuum. This means that the substrate can be cleaned and smoothed immediately prior to thin film growth, without exposing the sample to any source of contamination. Another source of surface contamination is water. In storage, the condensation of water vapour can not be prevented. Water reacts with MgO to produce  $\text{Mg}(\text{OH})_2$  [Liu et al., 1998]. This compound produces hillocks on the surface. The substrate is usually annealed to eliminate this contamination. This effectively removes the water, but leaves the hillocks behind. They contribute to the surface roughness. Thus, they can subsequently be removed with the methods described above.

Commonly, MgO substrate will contain more than one crystal domain. The deviation in domain orientation is only slight. Nonetheless it appears in  $\omega$ -curves (XRD). Low-angle  $\omega$ -curves usually have a single sharp peak. But for a multi-domain substrate, the peak splits up, and the peak width will increase to several tenths of a degree. It will also have more than one local maxima.

**Cr<sub>x</sub>Mo<sub>1-x</sub>/MgO heteroepitaxy**

The structure and morphology of thin epitaxial overlayers of MgO on lattice-matched interlayers of Cr<sub>0.7</sub>Mo<sub>0.3</sub> have been investigated [Chambers et al., 1995]. The films were grown by MBE. The alloy was grown at RT and annealed, while the MgO overlayer was grown at 550°C. High resolution transmission electron microscopy (TEM) and diffraction revealed a high degree of structural coherency at the interfaces. Cr<sub>0.7</sub>Mo<sub>0.3</sub> was found to grow in a layer-by-layer fashion on the MgO substrate, and the films exhibited extremely low mean roughness of 0.2 nm. However, the MgO overlayer grew in a three-dimensional mode with a mean roughness of 0.4 nm for a 1.4 nm thick film. Atomic force microscope (AFM) images also showed evidence of dispersed islands, that were a few nanometers high. The authors attributed this to a surface energy mismatch. That is a very likely explanation, although the surface energy data on which the argument was based, seems to have been incorrect. The authors refer to data for polycrystalline metals, which differ from the values for the (001) faces of crystalline metals. Nonetheless, the explanation may still be valid, as discussed in section 5.2.

# Chapter 4

## Experimental apparatus and method

In this chapter the instruments used for synthesis and characterization of ultra-thin films are described. The specifications of the magnetron sputtering discharge, in which the films were deposited are discussed. Structural characterization using X-Ray techniques is considered, and finally the measurement of the electrical resistivity using a four-point probe is described.

### 4.1 Magnetron sputtering discharge

The metal films used in the current study were deposited in a custom-built magnetron sputtering discharge. A photograph of the system is shown in Fig. 4.1. The vacuum chamber has three sputtering targets. A resistive heater stage is mounted under the substrate, and the substrate temperature is measured using a thermocouple. The system permits the simultaneous use of three sputtering targets, each of which has a separate power supply. For the experimental work described in the next chapter, binary metal alloy films were prepared by sputtering two targets simultaneously. The composition was controlled by adjusting the power applied to each target.

## 4.2 X-Ray Diffraction

X-Ray diffraction (XRD) is a commonly used to assess crystal quality and lattice parameters [Cullity, 1978, Warren, 1990]. X-Rays incident on the crystal are scattered elastically from the electrons of the atoms in the crystal. The electron density is periodic along the three crystal axis, and therefore, the superposition of scattered waves produces a diffraction pattern, that is closely related to this periodicity. The diffraction pattern exists on a sphere, but for thick samples only half of the sphere may be observed. Each combination of incident and diffracted wave vectors probes a certain plane in the crystal lattice, and corresponds to a point in three-dimensional Fourier space for electron density waves. The three-dimensional Fourier space is referred to as the reciprocal space. The coordinates in the reciprocal space are the

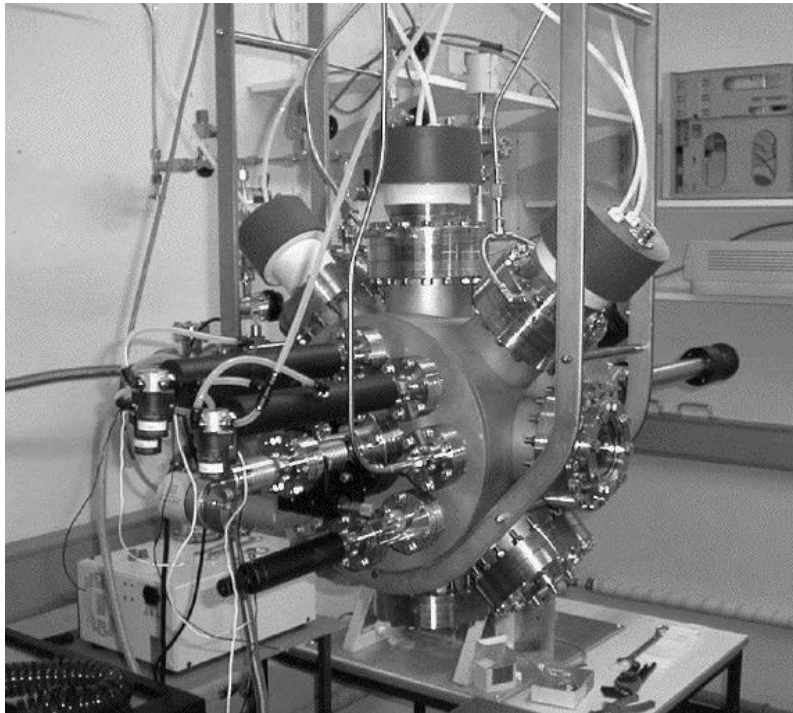


Figure 4.1: A magnetron sputtering discharge for ultra-thin film deposition. The vacuum chamber has three sputtering targets.

Miller indices of the plane.

A common measurement setup for what is called the Bragg-Brentano method is illustrated in Fig. 4.2. This method only evaluates the inter-planar distance perpendicular to the surface. The (001) Bragg peak gives the lattice constant,  $a$ , according to

$$a = \frac{\lambda}{2 \sin \theta}, \quad (4.1)$$

where  $\lambda$  is the wavelength of the X-Ray radiation and  $\theta$  is the incident angle as defined in Fig. 4.2. Thus, XRD provides information about the crystal structure. For a perfect crystal, between  $10^3 - 10^5$  planes contribute to the Bragg diffracted beam [Kittel, 1986, p. 29]. Therefore XRD probes the crystalline order deep into the crystal. However it can also be used to study thin film attributes. The position of the peaks gives information about the orientation of the film, and a small deviation from the anticipated position indicates strain. During growth, films may develop a mosaic structure. That means that it contains crystal segments of finite size. Usually the segments are of the same orientation, but exhibit a small deviation from

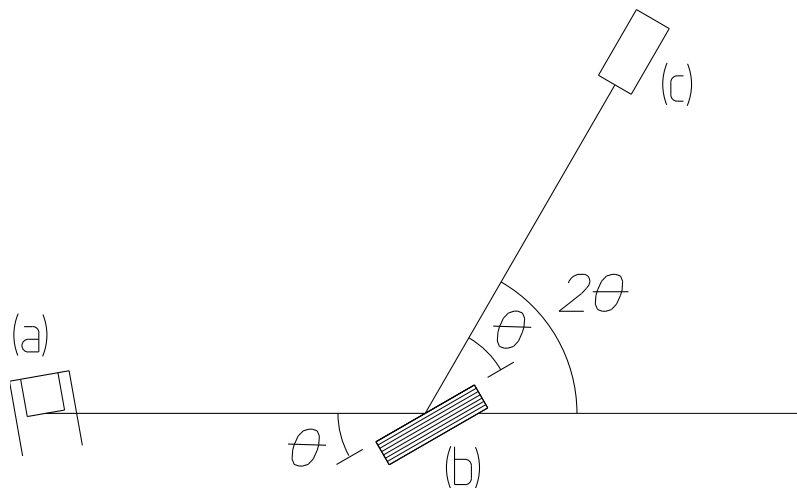


Figure 4.2: Apparatus for Bragg-Brentano XRD. (a) X-Ray source, (b) the sample, and (c) the detector.

the exact orientation dictated by the epitaxial relationship with the substrate. This is reflected in the width of the XRD peak. The mosaic block size,  $t$ , is given by [Cullity, 1978, p. 102]

$$t = \frac{0.9\lambda}{B \cos \theta_B}, \quad (4.2)$$

where  $B$  is the full-width-at-half-maximum (FWHM) of the Bragg peak in radians and  $\theta_B$  is the position of the Bragg peak.

### 4.3 X-Ray Reflectometry

The short wavelength of the X-Ray radiation also enables one to study microscopic details of surface roughness on comparable length scales [Sinha et al., 1988]. The scattering of radiation from rough surfaces has been described analytically by finding approximations for solving the standard equations of electromagnetic theory, while matching boundary conditions over a random surface. The measured scattering as a function of the incident angle is called X-Ray reflectometry (XRR). The scattered intensity falls rapidly with the angle so the XRR curve is only measured up to a small angle. Furthermore, XRR can be used to study thin film and multilayer properties [Holy et al., 1999, p. 191 - 219]. Typical XRR curves for thin films are shown in Fig. 5.2. Beyond the angle of total surface reflection, interference patterns due to scattering at the respective interfaces appear. The relative angular separation of the interference peaks gives information on film thickness, and the amplitude of the interference oscillations reflects the interface roughness. The surface scattering appears as an envelope for the interference oscillations, and thus the angular decay of the XRR curve provides information on the surface roughness. The XRR curve further depends on the complex dielectric constant of the film material, which reflects the density and adsorption coefficient. An analytic framework has been established

to describe the XRR curve facilitating computer simulation and curve fitting to the measured data.

## 4.4 Electrical resistance

The way in which resistivity changes with thickness was discussed in section 2.3. There it was assumed that the film was continuous. If a two-dimensional growth mode is not achieved, the film may reach a considerable thickness before it becomes continuous. That obscures the effect of the small thickness on the resistance. However, if the deposition rate is well defined, this can be used as an indicator whether or not the growth is two-dimensional. It can be problematic to achieve invariant conditions for thin film resistance measurements due to the contact resistance. This problem can be alleviated by using the four-point probe illustrated in Fig. 4.3 [Smith, 1995, p. 575 - 577]. A constant current is passed through the outer two contacts, and the resulting voltage at the two inner contacts is measured. If enough current flows to cause a significant voltage drop, and the input impedance

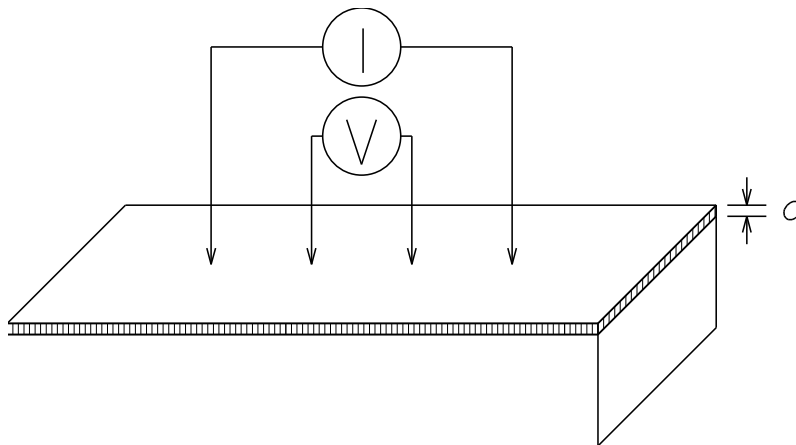


Figure 4.3: Four-point-probe resistance measurement setup. A constant current is passed between the two outer contacts, and the voltage is measured between the two inner contacts.

of the voltmeter is very high compared to the film resistance, the effects of contact resistance disappear. Usually point contacts clamped to the sample with a spring can be used.

# Chapter 5

## Experimental results

Here we describe the preparation of  $\text{Cr}_x\text{Mo}_{1-x}$  thin films in a magnetron sputtering discharge, and their characterization using X-Ray Diffraction and X-Ray Reflectometry. Based on the structural information, we determined the optimum growth temperature. At this optimum growth temperature ultra-thin films in the range of 1.8 to 70 ML thick were prepared. Using four-point-probe resistance measurements layer-by-layer growth was confirmed.

### 5.1 Experimental apparatus and method

The deposition of the films was performed in a custom built DC planar balanced magnetron sputtering discharge with a load-lock entry [Olafsson and Arnalds, 1999]. The base pressure was in the  $10^{-9} - 10^{-8}$  mbar range. Two separate targets of 99.98 % pure Cr and 99.95 % pure Mo were used, and a 99.999% pure Ar gas at  $4 \times 10^{-3}$  mbar. Polished MgO(001) substrates, with 0.5 nm RMS roughness were cleaned with acetone and methanol in ultrasonic baths prior to insertion into the vacuum chamber. Once under UHV, the substrates were out-gassed and annealed for 10 minutes at 750°C in order to bake water in the form of  $\text{Mg}(\text{OH})_2$  from the surface.

$\text{Cr}_x\text{Mo}_{1-x}$  films of thickness 55 - 59 nm were deposited on the substrates at growth temperatures ranging from room temperature (RT) to 800°C. The films were grown with the substrate holder at a floating potential.

Ex-situ X-Ray Diffraction (XRD) and X-Ray Reflectometry measurements were carried out using a Philips PW1710 Diffractometer with an angular resolution of 0.005°, using a Cu tube ( $\text{CuK}_\alpha$ ,  $\lambda = 1.5406$  nm). Fig. 5.1 shows a typical XRD scan. The film orientation and the out-of-plane lattice constant were evaluated using Bragg-Brentano scans, and the mosaic thickness of the film was calculated according to Eq. (4.2). Fig. 5.2 shows typical X-Ray Reflectometry scans and fits to the measured data. The film thickness, density, as well as the surface and interface roughness were evaluated by fitting X-Ray Reflectometry data using Philips WinGixa Software. This knowledge facilitated the calculation of the deposition rate,

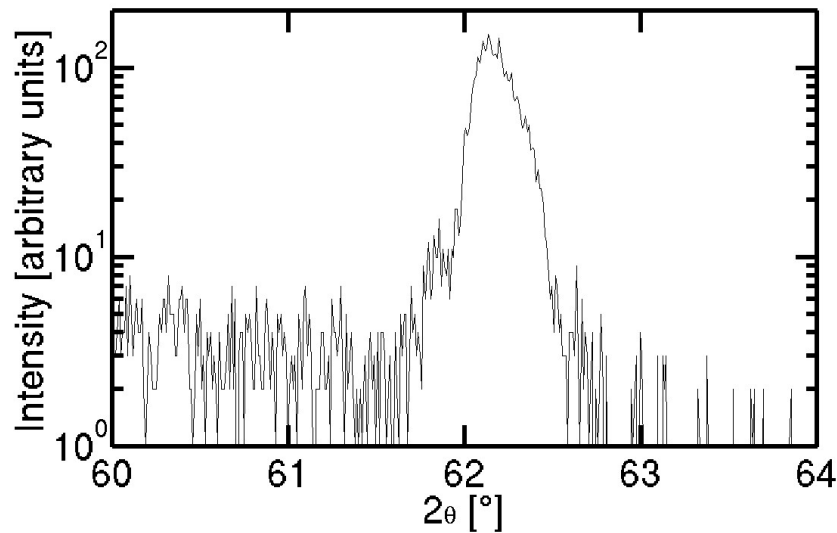


Figure 5.1: High angle X-Ray Diffraction measurement for a  $\text{Cr}_x\text{Mo}_{1-x}$  grown at 200°C, with  $x \approx 0.63$ .

and the assessment of the actual composition, and thus the out-of-plane strain.

Using the optimum growth temperature determined from the structural data, ultra-thin films (1.8 - 70 ML) were grown. A constant growth rate was assumed and the nominal thickness of the ultra-thin films was calculated as the product of the deposition time and the growth rate. The resistance of the films was measured using a Keithley 199 precision multimeter in four-point-probe mode.

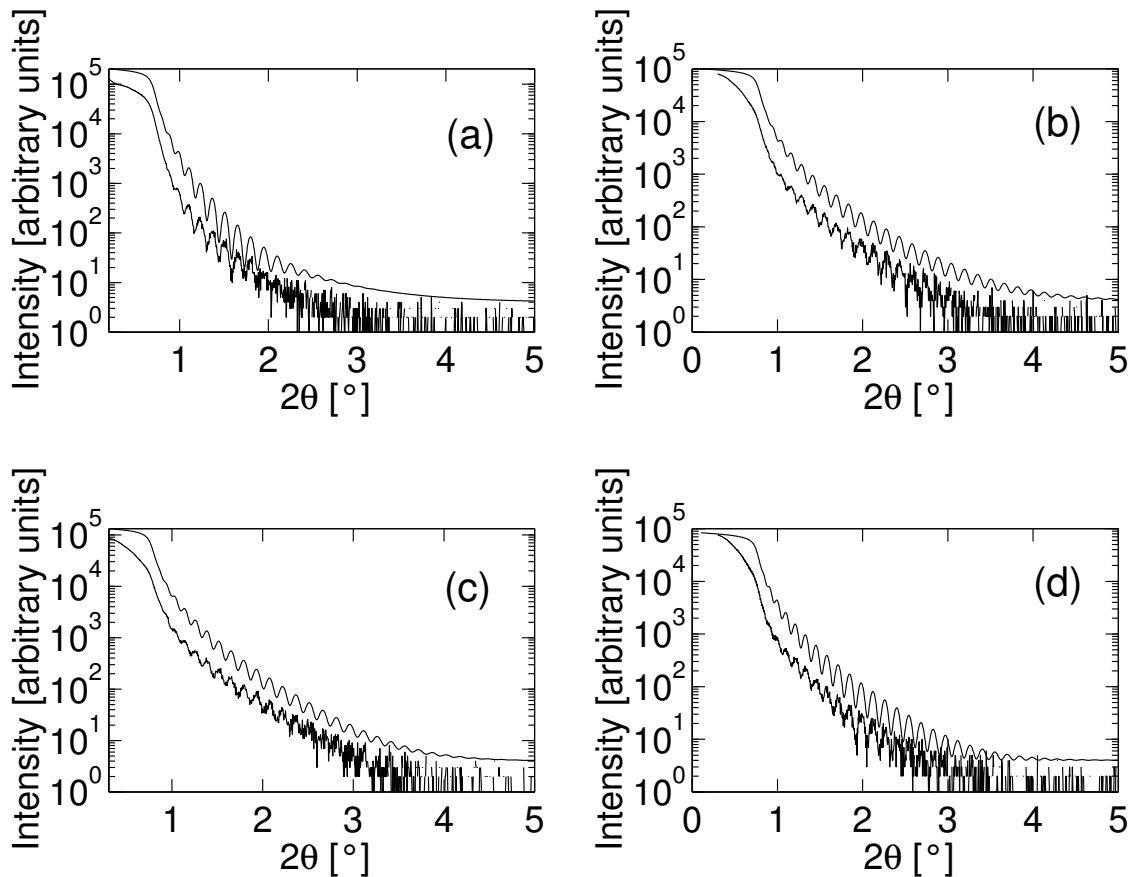


Figure 5.2: X-Ray Reflectometry curves for  $\text{Cr}_x\text{Mo}_{1-x}$  films, with  $x \approx 0.63$ , grown at different temperatures. (a) RT, (b) 200°C, (c) 500°C, and (d) 800°C. In each figure the measured data is shown as the lower curve, and a fit to the measured data is shown as the upper curve. The curves are vertically offset for clarity.

## 5.2 Results and discussion

Fig. 5.1 shows XRD data for a  $\text{Cr}_x\text{Mo}_{1-x}$  sample grown at  $200^\circ\text{C}$ , with  $x \approx 0.63$ . X-Ray Reflectometry data for the same sample is shown in Fig. 5.2 (b). The com-

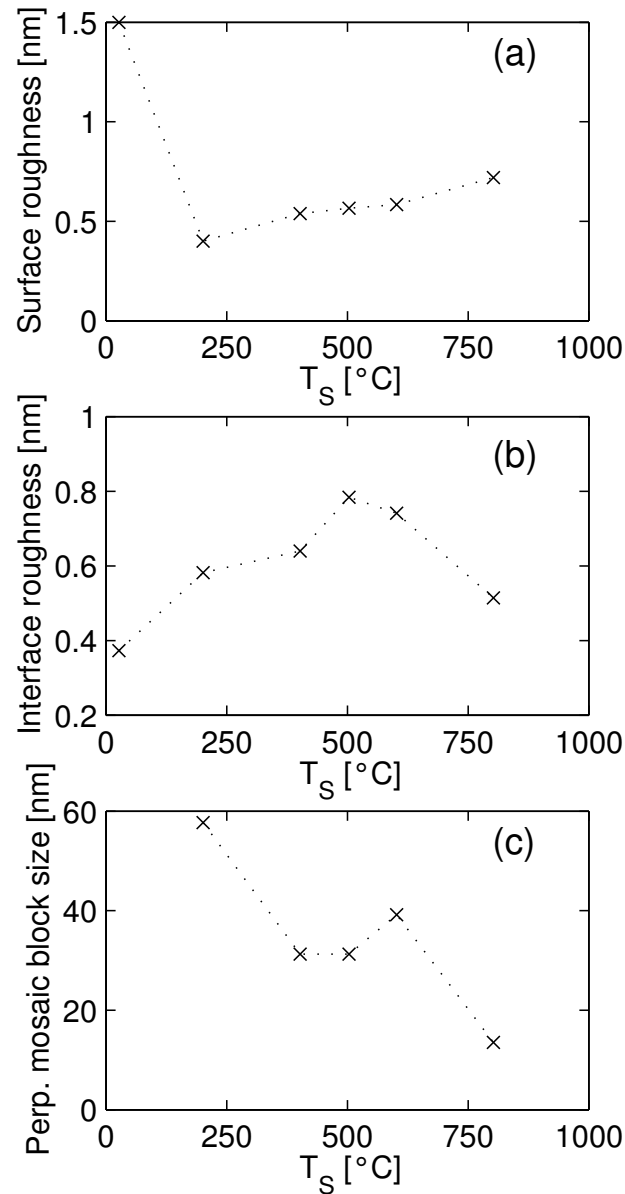


Figure 5.3: Film properties for a  $\text{Cr}_x\text{Mo}_{1-x}$  alloy, with  $x \simeq 0.63$ . (a) Film surface roughness, (b) film/substrate interface roughness, and (c) mosaic thickness in the direction perpendicular to the substrate surface, versus growth temperature.

position was assessed using a fit to the data, which is also shown in the figure. Figs. 5.2 (a), (c) and (d) show X-Ray Reflectometry data for  $\text{Cr}_x\text{Mo}_{1-x}$  samples grown at RT, 500°C, and 800°C, respectively. Figs. 5.3 and 5.4 show the collected morphological and structural information gained from the XRD and X-Ray Reflectometry

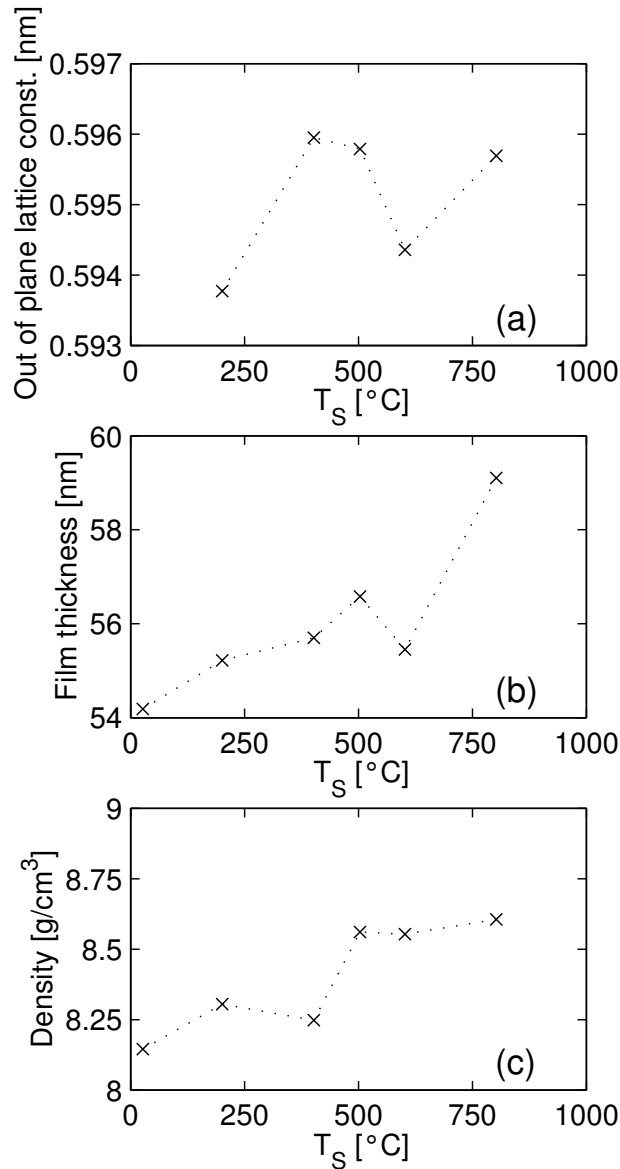


Figure 5.4: Film properties for a  $\text{Cr}_x\text{Mo}_{1-x}$  alloy, with  $x \approx 0.63$ . (a) Out-of-plane lattice constant, i.e. in the direction perpendicular to the substrate surface, (b) film thickness, and (c) film density, versus growth temperature.

measurements as a function of growth temperature. Fig. 5.3 (a) shows the film surface roughness, Fig. 5.3 (b) shows film/substrate interface roughness, and Fig. 5.3 (c) shows the mosaic thickness in the direction perpendicular to the substrate surface. Fig 5.4 (a) shows the out-of-plane lattice constant, i.e. in the direction perpendicular to the substrate surface, Fig. 5.4 (b) shows the film thickness, and Fig. 5.4 (c) shows the film density.

For samples prepared at room temperature (RT) an X-Ray Diffraction peak could not be detected indicating a non-crystalline film. At RT surface diffusion is too slow relative to the growth rate for the atoms to be able to form a periodic lattice, thus the absence of a diffraction peak for samples grown at RT. The lack of crystallinity is accompanied with a high surface roughness, as can be seen in Fig. 5.3 (a) and a slightly lowered density, as can be seen in Fig. 5.4 (c). At a growth temperature of 200°C the surface diffusion is sufficient for the formation of a high quality crystal with a pronounced diffraction peak and a mosaic thickness perpendicular to the substrate surface approximately equal to the total film thickness as can be seen by comparing the corresponding values in Figs. 5.3 (c) and 5.4 (b). Furthermore the film exhibits extremely low surface roughness, lower than that of the interface. As the growth temperature is raised the surface and interface roughness increases, as shown in Fig. 5.3 (a) and (b) respectively, and the mosaic thickness decreases, as indicated in Fig. 5.3 (c). Also the out-of-plane lattice constant increases, as seen in Fig. 5.4 (a), which is reflected in an increased film thickness, as portrayed in Fig. 5.4 (b). This is an indication of film strain resulting from the different thermal expansion coefficients of the MgO substrate and the  $\text{Cr}_x\text{Mo}_{1-x}$  film. Relative integrated thermal expansion is given by  $\epsilon = (L(T) - L(293))/L(293)$  where  $T$  is the temperature in Kelvin. For growth temperature  $T = 500^\circ\text{C} = 773\text{K}$  considerable film strain was observed. The relative integrated thermal expansion of the materials

in the current system at this temperature is:  $\epsilon_{\text{Cr}} = 4.236 \times 10^{-3}\text{K}^{-1}$  [Gray, 1972, p. 4-123],  $\epsilon_{\text{Mo}} = 2.556 \times 10^{-3}\text{K}^{-1}$  [Gray, 1972, p. 4-127], and  $\epsilon_{\text{MgO}} = 0.615 \times 10^{-3}\text{K}^{-1}$  [Gray, 1972, p. 4-138]. Although the behavior of a binary metal alloy can have a complex relation to the properties of its elemental constituents, we can make a qualitative assessment by assuming that the thermal expansion coefficient of the alloy is of the same order of magnitude as that of the constituents. That way we can argue that the thermal expansion coefficient of the alloy is greater than that of MgO. Thus the film contracts to a greater extent than the substrate when brought down to room temperature, resulting in compressive strain in the substrate plane and tensile strain in the direction perpendicular to the substrate plane [Smith, 1995, p. 186 - 193]. However, the compression in two dimensions can not fully be compensated for by the one-dimensional expansion and thus an increase in density results, as evident in Fig. 5.4 (c). This may be one of the reasons for the degradation of the film properties with increased growth temperature, since film stress affects the interface energy and also induces dislocation defects as a means of stress relaxation. As noted above, all the film properties reached their optimal value for films grown at 200°C, and thus we conclude that this is the optimal growth temperature for the current system.

The fact that optimal growth conditions are realized at a relatively low growth temperature may be surprising. It is however in agreement with the observations of Thornton [Thornton, 1974], which relate the optimal growth temperature to the melting point of the film material. According to Thornton's schematic illustration in Fig. 2.6, the optimum lies within the range 110 - 493°C, given the approximate melting point of the alloy  $\text{Cr}_{0.7}\text{Mo}_{0.3}$ ,  $T_m = 1915^\circ\text{C}$  taken from the Cr-Mo phase diagram [Ventrakaman and Neumann, 1990]. Thornton's observations were for elemental metals. The binary metal alloy used in the present study has a miscibility gap be-

low roughly  $800^\circ\text{C}$ , which causes a tendency towards segregation during (extensive) thermal treatments at temperatures below  $800^\circ\text{C}$ , due to increased bulk diffusion compared to RT. For this reason the material may exhibit fundamentally different growth behavior. Films prepared by Chambers et al. [Chambers et al., 1995] were grown with MBE at RT and annealed for a few minutes at  $550^\circ\text{C}$ , were reported to have similar properties. The high energy of the incident particles in the magnetron sputtering process can affect the surface diffusion of atoms being incorporated in the film [Wei et al., 2000], thus possibly permitting a good crystal to be formed at a considerably lower temperature than would be achieved with other methods. This is also in agreement with observations elsewhere [Byon et al., 2003, Menendez et al., 1998]. This is especially advantageous in the current system because of the the miscibility gap discussed above.

Fig. 5.5 shows the electrical resistance versus thickness for  $\text{Cr}_x\text{Mo}_{1-x}$  films, hav-

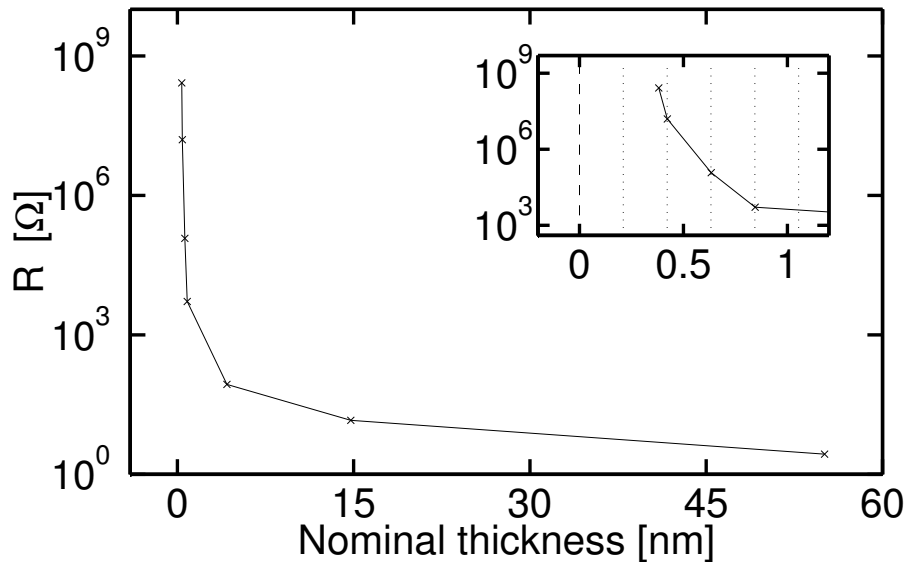


Figure 5.5: Electrical resistance versus thickness for  $\text{Cr}_x\text{Mo}_{1-x}$  films, having  $x \approx 0.63$ , deposited at  $200^\circ\text{C}$  growth temperature. The inset is a magnification of the behavior in the subnanometer range. The dotted vertical lines indicate the nominal thickness of subsequent monolayer.

ing  $x \approx 0.63$ , grown at  $200^\circ\text{C}$ . The inset shows a magnification of the behavior at sub-nanometer thickness. The surface resistance of the substrate was found to be above  $1\text{ G}\Omega$ . Island growth is characterized by a plateau region at the low thickness limit on the corresponding resistance versus thickness curve [Seal et al., 2003]. This is because the resistance remains high until the onset of island coalescence, which enables metallic conduction. It has been estimated that this commonly occurs at a fractional coverage of 0.65 [Seal et al., 2003]. The plateau is followed by a sudden drop of several orders of magnitude in electrical resistance. The midpoint of the drop is usually taken as the coalescence thickness. Beyond this thickness the resistance is initially dominated by size effects, and then scattering by thermal lattice vibration and impurities. As can be seen from the inset in Fig. 5.5 the resistance versus thickness curve still has the form characteristic for size dependent electrical resistance [Trivedi and Ashcroft, 1988] down to 1.8 ML nominal thickness. The curve does not exhibit a plateau region or a discrete drop in electrical resistance indicating that the film becomes continuous at least before the second ML is formed. Thus we conclude that the films grow in a layer-by-layer fashion.

Such growth can be expected if the sum of the interface energy and film material surface energy is lower than the substrate surface energy [Smith, 1995, p. 143]. The theoretically determined surface energy of  $\text{MgO}(001)$  is  $2.64\text{ J/m}^2$  [Gibson et al., 1992], that of  $\text{Mo}(001)$  is  $3.84\text{ J/m}^2$  [Vitos et al., 1998], and that of  $\text{Cr}(001)$  is  $3.98\text{ J/m}^2$  [Vitos et al., 1998]. Thus, the surface energy of Mo and Cr is considerably higher than that of MgO, seemingly contradictory to the fact that the Cr-Mo alloy was found to grow in a layer-by-layer fashion. There are two possible explanations. Firstly, the surface energy of a binary metal alloy depends on the composition, and can assume values that are lower than that of either constituent [Christensen et al., 1997]. Secondly, the theoretical values may be inaccurate. The surface energy of  $\text{Mo}(001)$

has been experimentally evaluated as  $2.93 \text{ J/m}^2$  [Che et al., 1998]. If this is the correct value, a negative interface energy may be sufficient to induce layer-by-layer growth. This is in agreement with the conclusions made by Chambers et al. on the basis of RHEED and surface roughness measurements, although their argument was based on different surface energy values [Chambers et al., 1995].

Layer-by-layer growth allows the preparation of ultra-thin films where the conductance is only limited by quantum mechanical properties and are not affected by island formation and diffuse surface scattering. Also the absence of perpendicular mosaic boundaries as discussed above minimizes the effects of boundary scattering.

From the above discussion it is clear that the surface energy of  $\text{Cr}_x\text{Mo}_{1-x}$  is close enough to that of MgO to permit layer-by-layer growth. The surface energy of the alloy is likely to be higher than that of the substrate because both the alloy constituents have considerably higher surface energies. If these assumptions are correct, this would have a positive influence on MgO growth on the  $\text{Cr}_x\text{Mo}_{1-x}$  layer. However that is contradictory to the results of Chambers et al. [Chambers et al., 1995]. They grew MgO films on  $\text{Cr}_{0.7}\text{Mo}_{0.3}$  using MBE, and attempted to influence the growth process by controlling the substrate temperature. The resulting films were found to consist of dispersed islands. As discussed in earlier chapters, the relation can be quite complex. Therefore, it is not impossible that smooth MgO films may be deposited on  $\text{Cr}_x\text{Mo}_{1-x}$  under different growth conditions. Also, if the alloy surface energy is very sensitive to the composition, it may be beneficial to match the surface energy rather than the lattice constant. This will be the subject of further research.

# Chapter 6

## Summary

The importance of structural perfection was made clear in terms of the theory of metallic conduction and insulator leakage currents. The use of a  $\text{Cr}_x\text{Mo}_{1-x}$  binary metal alloy was shown to produce high quality crystalline films on an MgO substrate with low surface roughness and a sharp interface with the substrate. Furthermore, the deposition of ultra-thin  $\text{Cr}_x\text{Mo}_{1-x}$  films on MgO was demonstrated with thickness down to 1.8 monoatomic layers. The resistance of these ultra-thin films clearly reflected the effect of the small thickness.

# Acknowledgements

My supervisors, Dr. Jón Tómas Guðmundsson, Dr. Sveinn Ólafsson and Dr. Kristinn Johnsen provided many helpful comments on the thesis and discussions on the subject. I am very grateful for their support. Dr. Ragnar K. Ásmundsson also gave insightful comments on the thesis. I appreciate the cooperation of Árni Sigurður Ingason in setting up the X-Ray measurement system, as well as the help of Halldór Svavarsson in substrate preparation and discussions on chemical properties. Furthermore, proofreading of the thesis by Friðrik Magnus is appreciated. I would like to express my gratitude to my friend and fellow student Kristinn B. Gylfason for many fruitful conversations on physics, electronics, research methods and many other subjects. Finally I would like to thank my family for endless patience and support.

This work was partially supported by Lyfjathroun hf., Biopharmaceutical Research, Reykjavik, Iceland, and the University of Iceland Research Fund.

# Bibliography

- [Alivisatos, 1996] Alivisatos, A. P. (1996). Semiconductor clusters, nanocrystals, and quantum dots. *Science*, 271:933 – 937.
- [Barnham and Vvedensky, 2001] Barnham, K. and Vvedensky, D. (2001). *Low-dimensional semiconductor structures*. Cambridge University Press, Cambridge.
- [Bauer and van der Merwe, 1986] Bauer, E. and van der Merwe, J. H. (1986). Structure and growth of crystalline superlattices: From monolayer to superlattice. *Physical Review B*, 33:3657 – 3671.
- [Byon et al., 2003] Byon, E., Oates, T. W. H., and Anders, A. (2003). Coalescence of nanometer silver islands on oxides grown by filtered cathodic arc deposition. *Applied Physics Letters*, 82:1634 – 1636.
- [Caceres et al., 2002] Caceres, D., Colera, I., Vergara, I., Gonzalez, R., and Roman, E. (2002). Characterization of MgO thin films grown by rf-sputtering. *Vacuum*, 67:577 – 581.
- [Chambers, 2000] Chambers, S. A. (2000). Epitaxial growth and properties of thin film oxides. *Surface Science Reports*, 39:105 – 180.
- [Chambers et al., 1995] Chambers, S. A., Gao, Y., and Liang, Y. (1995). The early stages of MgO epitaxy on lattice-matched Cr<sub>0.7</sub>Mo<sub>0.3</sub>(001). *Surface Science*, 339:297 – 309.
- [Chambers et al., 1994] Chambers, S. A., Tran, T. T., and Hileman, T. A. (1994). Molecular beam homoepitaxial growth of MgO(001). *Journal of Materials Research*, 9:2944 – 2952.
- [Chapin, 1974] Chapin, J. S. (January 1974). The planar magnetron. *Research/Development*, pages 37 – 40.

- [Che et al., 1998] Che, J. G., Chan, C. T., Jian, W.-E., and Leung, T. C. (1998). Surface atomic structures, surface energies and equilibrium crystal shape of molybdenum. *Physical Review B*, 57:1875 – 1880.
- [Cheng et al., 2003] Cheng, Y. H., Kupfer, H., Richter, F., Giegengack, H., and Hoyer, W. (2003). Structure and secondary electron emission properties of MgO films deposited by pulsed mid-frequency magnetron sputtering. *Journal of Applied Physics*, 93:1422 – 1427.
- [Cheng et al., 2002] Cheng, Y. H., Kupfer, H., Richter, F., and Paraian, A. M. (2002). Deposition of MgO films by pulsed mid-frequency magnetron sputtering. *Applied Surface Science*, 200:117 – 124.
- [Christensen et al., 1997] Christensen, A., Ruban, A. V., Stoltze, P., Jacobsen, K. W., Skriver, H. L., Norskov, J. K., and Besenbacher, F. (1997). Phase diagrams for surface alloy. *Physical Review B*, 56:5822 – 5834.
- [Cullity, 1978] Cullity, B. D. (1978). *Elements of X-Ray Diffraction, 2nd ed.* Addison-Wesley, Reading, Massachusetts.
- [Davies and Betts, 1994] Davies, P. C. W. and Betts, D. S. (1994). *Quantum Mechanics.* Chapman & Hall, London.
- [Fuchs, 1938] Fuchs, K. (1938). The conductivity of thin metallic films according to the electron theory of metals. *Proceedings of the Cambridge Philosophical Society*, 34:100 – 108.
- [Gibson et al., 1992] Gibson, A., Haydock, R., and Lafemina, J. P. (1992). Electronic-structure and relative stability of the MgO(001) and MgO(111) surfaces. *Journal of Vacuum Science and Technology A*, 10:2361 – 2366.
- [Gray, 1972] Gray, D. E., editor (1972). *American Institute of Physics Handbook.* American Institute of Physics, New York.
- [Hilleringmann, 1999] Hilleringmann, U. (1999). *Silizium-Halbleitertechnologie.* Teubner Studienbuecher, Stuttgart.
- [Holy et al., 1999] Holy, V., Pietsch, U., and Baumbach, T. (1999). *High-Resolution X-Ray Scattering from Thin Films and Multilayers.* Springer-Verlag, Berlin.

- [Hori, 1997] Hori, T. (1997). *Gate Dielectrics and MOS ULSIs*. Springer Verlag, Berlin.
- [Jalochowski and Bauer, 1988] Jalochowski, M. and Bauer, E. (1988). Quantum size and surface effects in the electrical resistivity and high-energy electron reflectivity of ultrathin lead films. *Physical Review B*, 38:5272 – 5280.
- [Jouan and Lemperiere, 1994] Jouan, P.-Y. and Lemperiere, G. (1994). Study of a rf planar magnetron sputtering discharge: Discharge characteristics and plasma diagnostics. *Vacuum*, 45:89–95.
- [Kado, 1996] Kado, T. (1996). Epitaxial superlattices of TiAg alloy/MgO grown on MgO(001). *Applied Physics Letters*, 69:1293 – 1395.
- [Kado et al., 1999] Kado, T., Nakamura, K., and Matsuura, M. (1999). Structural analysis of epitaxial TiAg/MgO superlattices prepared by multi-evaporation. *Thin Solid Films*, 343 – 344:545 – 549.
- [Kawamura et al., 2000] Kawamura, M., Mashima, T., Abe, Y., and Sasaki, K. (2000). Formation of ultra-thin continuous Pt and Al films by RF sputtering. *Thin Solid Films*, 377 – 378:537 – 542.
- [Kelly et al., 2000] Kelly, P. J., Henderson, P. S., Arnell, R. D., Roche, G. A., and Carter, D. (2000). Reactive pulsed magnetron sputtering process for alumina films. *Journal of Vacuum Science and Technology A*, 18:2890 – 2896.
- [Kiguchi et al., 2002] Kiguchi, M., Goto, T., Saiki, K., Sasaki, T., Iwasawa, Y., and Koma, A. (2002). Atomic and electronic structures of MgO/Ag(001) heterointerface. *Surface Science*, 512:97 – 106.
- [Kittel, 1986] Kittel, C. (1986). *Introduction to Solid State Physics*. John Wiley & Sons, New York.
- [Kundu and Murata, 2002] Kundu, M. and Murata, Y. (2002). Growth of single-crystal SiO<sub>2</sub> film on Ni(1 1 1) surface. *Applied Physics Letters*, 80:1921 – 1923.
- [Lieberman and Lichtenberg, 1994] Lieberman, M. A. and Lichtenberg, A. J. (1994). *Principles of Plasma Discharges and Materials Processing*. John Wiley & Sons, New York.

- [Liu et al., 2001] Liu, H. D., Zhao, Y. P., Ramanath, G., Murarka, S. P., and Wang, G. C. (2001). Thickness dependent electrical resistivity of ultrathin ( $< 40$  nm) Cu films. *Thin Solid Films*, 384:151 – 156.
- [Liu et al., 1998] Liu, P., Kendelewicz, T., Brown, Jr., G. E., and Parks, G. A. (1998). Reaction of water with MgO(100) surface. Part I: Synchrotron X-ray photoemission studies of low-defect surfaces. *Surface Science*, 412 - 413:287 – 314.
- [Maniv and Westwood, 1980] Maniv, S. and Westwood, W. D. (1980). Discharge characteristics for magnetron sputtering of Al in Ar and Ar/O<sub>2</sub> mixtures. *Journal of Vacuum Science and Technology A*, 17:743 – 751.
- [Menendez et al., 1998] Menendez, J. L., Caro, P., and Cebollada, A. (1998). Epitaxy, strain and morphology of low pressure Ar pressure sputtered Pt thin films. *Journal of Crystal Growth*, 192:164 – 174.
- [Morawe and Zabel, 1995] Morawe, C. and Zabel, H. (1995). Thermal stability and superlattice formation of sputtered platinum/alumina multilayers. *Applied Physics Letters*, 67:2612 – 2614.
- [Muller et al., 1999] Muller, D. A., Sorsch, T., Moccio, S., Baumann, F. H., Evans-Lutterodt, K., and Timp, G. (1999). The electronic structure at the atomic scale of ultrathin oxides. *Nature*, 399:758 – 761.
- [Murata et al., 2001a] Murata, Y., Kundu, M., Ikeda, A., Fujimoto, H., and Matsumoto, M. (2001a). Layer growth of Pt on  $\alpha$ -Al<sub>2</sub>O<sub>3</sub>/Ru(0 0 0 1). *Surface Science*, 493:114 – 119.
- [Murata et al., 2001b] Murata, Y., Nagata, K., Fujimoto, H., Sakurai, T., Okada, M., and Ebe, Y. (2001b). Electronic property of thin single-crystal films of  $\alpha$ -Al<sub>2</sub>O<sub>3</sub> on Ru(0 0 0 1). *Journal of the Physical Society of Japan*, 70:793 – 796.
- [Namba, 1970] Namba, Y. (1970). Resistivity and temperature coefficient of thin metal films with rough surface. *Japanese Journal of Applied Physics*, 9:1326 – 1329.
- [Olafsson and Arnalds, 1999] Olafsson, S. and Arnalds, U. B. (1999). Spætun og ræktun með segulspætu. In Ólafsson, A., editor, *Eðlisfræði á Íslandi IX*, pages 143–152, Reykjavík. Eðlisfræðifélag Íslands.

- [Ostadal and Hill, 2001] Ostadal, I. and Hill, R. M. (2001). DC conduction of stable ultrathin Pt films below the percolation threshold. *Physical Review B*, 64:33404.
- [Rickart et al., 2001] Rickart, M., Roos, B. F. P., Mewes, T., Jorzick, J., Demokritov, S. O., and Hillebrands, B. (2001). Morphology of epitaxial metallic layers on MgO substrates: Influence of submonolayer carbon contamination. *Surface Science*, 495:68 – 76.
- [Schiller et al., 1993] Schiller, S., Goedicke, K., Reschke, J., Kirchhoff, V., Schneider, S., and Milde, F. (1993). Pulsed magnetron sputter technology. *Surface & Coatings Technology*, 61:31 – 337.
- [Schintke et al., 2001] Schintke, S., Messerli, S., Pivetta, M., Patthey, F., Libioulle, L., Stengel, M., De Vita, A., and Schneider, W.-D. (2001). Insulator at the ultrathin limit: MgO on Ag(001). *Physical Review Letters*, 87:276801.
- [Schroeder et al., 2001] Schroeder, T., Hammoudeh, A., Pykavy, M., Magg, N., Adelt, M., Baeumer, M., and Freund, H. J. (2001). Single crystalline silicon dioxide films on Mo(1 1 2). *Solid-State Electronics*, 45:1471 – 1478.
- [Seal et al., 2003] Seal, K., Nelson, M. A., Ying, Z. C., Genov, D. A., Sarychev, A. K., and Shalaev, V. M. (2003). Growth, morphology, and optical and electrical properties of semicontinuous metallic films. *Physical Review B*, 67:35318.
- [Sellers, 1998] Sellers, J. (1998). Asymmetric bipolar pulsed DC: The enabling technology for reactive PVD. *Surface & Coatings Technology*, 98:1245 – 1250.
- [Sinha et al., 1988] Sinha, S. K., Sirota, E. B., and Garoff, S. (1988). X-ray and neutron scattering from rough surfaces. *Physical Review B*, 38:2297 – 2311.
- [Smith, 1995] Smith, D. L. (1995). *Thin-Film Deposition: Principles and Practice*. McGraw-Hill, New York.
- [Somorjai, 1994] Somorjai, G. A. (1994). *Introduction to Surface Chemistry and Catalysis*. John Wiley & Sons, New York.
- [Sondheimer, 1952] Sondheimer, E. H. (1952). The mean free path of electrons in metals. *Advances in Physics*, 1:1 – 39.

- [Stampe and Kennedy, 1998] Stampe, P. A. and Kennedy, R. J. (1998). Growth of MgO on Si(100) and GaAs(100) by laser ablation. *Thin Solid Films*, 326:63 – 66.
- [Thornton, 1974] Thornton, J. A. (1974). Influence of apparatus geometry and deposition conditions on the structure and topography of thick sputtered coatings. *Journal of Vacuum Science and Technology*, 11:666 – 670.
- [Thornton, 1986] Thornton, J. A. (1986). The microstructure of sputter-deposited coatings. *Journal of Vacuum Science and Technology A*, 4:3059 – 3065.
- [Toroczkai and Williams, 1999] Toroczkai, Z. and Williams, E. D. (1999). Nanoscale fluctuations at solid surfaces. *Physics Today*, 52:24 – 28.
- [Trivedi and Ashcroft, 1988] Trivedi, N. and Ashcroft, N. W. (1988). Quantum size effects in transport properties of metallic films. *Physical Review B*, 38:12298 – 12309.
- [Valeri et al., 2002a] Valeri, S., Altieri, S., delPennino, U., diBona, A., Luches, P., and Rota, A. (2002a). Scanning tunneling microscopy of MgO ultrathin films on Ag(001). *Physical Review B*, 65:245410.
- [Valeri et al., 2001] Valeri, S., Altieri, S., di Bona, A., Giovanardi, C., and Moia, T. S. (2001). Structural study of thin MgO layers on Ag(001) prepared by either MBE or sputter deposition. *Thin Solid Films*, 400:16 – 21.
- [Valeri et al., 2002b] Valeri, S., Altieri, S., diBona, A., Luches, P., Giovanardi, C., and Moia, T. S. (2002b). Thickness-dependent strain in epitaxial MgO layers on Ag(001). *Surface Science*, 517 – 510:311 – 317.
- [Ventrakaman and Neumann, 1990] Ventrakaman, M. and Neumann, J. P. (1990). Chromium-Molybdenum. In Massalski, T. B., editor, *Binary Alloy Phase Diagrams*, volume 2, pages 1293 – 1294. ASM International, Materials Park, Ohio, 2 edition.
- [Vitos et al., 1998] Vitos, L., Ruban, A. V., Skriver, H. L., and Kollar, J. (1998). The surface energy of metals. *Surface Science*, 411:186 – 202.
- [Waits, 1978] Waits, R. K. (1978). Planar magnetron sputtering. *Journal of Vacuum Science and Technology*, 15:179 – 187.

- [Wang et al., 2000] Wang, S. G., Tian, E. K., and Lung, C. W. (2000). Surface energy of arbitrary crystal planes of bcc and fcc solids. *Journal of the Physics and Chemistry of Solids*, 61:1295 – 1300.
- [Warren, 1990] Warren, B. E. (1990). *X-Ray Diffraction*. Dover, New York.
- [Wei et al., 2000] Wei, H., Liu, Z., and Yao, K. (2000). The influence of the incidence energy of deposited particles on the growth morphology of thin films. *Vacuum*, 57:87 – 97.
- [Wollschlager et al., 1999] Wollschlager, J., Viernow, J., Tegenkamp, C., Erdos, D., Schroder, K. M., and Pfnur, H. (1999). Stoichiometry and morphology of MgO films grown reactively on Ag(100). *Applied Surface Science*, 142:129 – 134.
- [Zandvliet et al., 2001] Zandvliet, H. J. W., Poelsema, D., and Swartzentruber, B. S. (2001). Diffusion on semiconductor surfaces. *Physics Today*, 54:40 – 45.
- [Zhang and Lagally, 1997] Zhang, Z. and Lagally, M. G. (1997). Atomistic processes in the early stages of thin-film growth. *Science*, 276:377 – 383.